

1 **Discontinuous electrical conductivity across the Yarlung**
2 **Zangbo Suture, Southern Tibet, implies a barrier to channel**
3 **flow**

4 **Jessica E. Spratt¹**

5 Department of Earth Sciences, Syracuse University, Syracuse, New York

6
7 **Alan G. Jones²**

8 Geological Survey of Canada, Ottawa, Canada

9
10 **Simon L. Klemperer**

11 Department of Geophysics, Stanford University, Stanford, California

12
13 **W. Wei**

14 China University of Geosciences, Beijing, China

15
16 **INDEPTH MT Team^{*}**

17
18 *Dedication:* K. Douglas Nelson passed away unexpectedly on August 17, 2002, and is still sorely missed.
19 Jessica Spratt was Doug's graduate student at the time of his death. Projects like INDEPTH are not hugely
20 successful without an inspirational leader who has vision, insight, purpose and drive, and are not immense
21 fun without that leader also having patience and a great sense of humor. Doug had all of those qualities and
22 we consider ourselves very fortunate to have worked with him. We dedicate this paper to Doug's memory.

23
24 ¹Now at: Wakefield, Quebec, Canada.

25 ²Now at: Dublin Institute for Advanced Studies, Dublin 2, Ireland.

26 ^{*}Other members of the INDEPTH MT Team are: H. Tan, S. Jin, M. Deng, China University of Geosciences,
27 Beijing, China; J.R. Booker, University of Washington, Seattle, Washington; P. Bedrosian, formerly
28 University of Washington, now at USGS, Denver.

Abstract

31 Project INDEPTH (International Deep Profiling of Tibet and the Himalaya)
32 magnetotelluric (MT) surveys crossed the India-Asia collision zone, the Yarlung-Zangbo
33 suture (YZS, also known as the Indus-Tsangpo suture), at ~90 °E longitude in 1995, and at
34 ~92 °E in 2001. Our re-analyses and re-modeling of these data provide new images of the YZS
35 that show significant variation in conductivity structure along the profiles, across the orogen.
36 Focused inversions of the MT data in the vicinity of the YZS show more structure within the
37 upper crust than previous smoother models, and the near-surface conductors help locate the
38 South Tibetan Detachment, Renbu-Zedong thrust and Gangdese thrust.

39 Comparison of the two parallel profiles shows remarkable along-strike similarity of
40 several conductors and resistors, attesting to the regional nature of the processes of
41 conductivity enhancement within the collision. On both profiles, in contrast to prior models,
42 the upper-crustal conductors south of the YZS are spatially isolated and are not connected to
43 the mid-crustal conductors observed at and north of the YZS. Consistent with prior
44 interpretations, the strong mid-crustal conductor north of the YZS likely represents partial melt
45 and indicates a weak mid-to-lower crust that greatly affects rheology and deformation
46 processes of Tibet. However, this inferred partial melt cannot continue unbroken beneath and
47 south of the YZS. No continuous melt-weakened layer, as expected for ongoing channel-flow
48 extrusion of the Himalaya, is continuously present from the Lhasa Block of southernmost Tibet
49 into the Tethyan Himalaya. Geodynamic models have to be re-assessed to accommodate this
50 new observation.

51 **Key words:**

52 India-Asia collision, Yarlung-Zangbo suture, Indus-Tsangpo suture, magnetotellurics,
53 electrical resistivity

54 **Index Terms:**

55 0905 Continental structures

56 8108 Continental tectonics: compressional

57 8120 Dynamics of lithosphere and mantle: general

58 8150 Plate boundary: general

59 9320 Asia

60 **1. Introduction**

61 The Himalaya-Tibetan Plateau provides a universal benchmark for testing theories on
62 processes of continental collision. Tibet has reached an average elevation of about 5 km above
63 sea level with an average crustal thickness of about 70 km from the Himalaya to the Kunlun
64 mountains (Figure 1) [e.g., *Mechie et al.*, 2011], resulting from continent-continent collision
65 between India and Asia [*Argand*, 1924]. However, despite it being the type example of
66 continental collision, the details of the processes are inadequately known and even more poorly
67 understood.

68 Project INDEPTH has been collecting geophysical data across the Himalaya-Tibetan
69 Plateau since 1992 [*Zhao et al.*, 1993], with the role of fluids in orogenesis as one of the main
70 objectives since the initiation of the second phase of INDEPTH [*Nelson et al.*, 1996].
71 Determining the nature and distribution of fluids within the lithosphere in active orogens is
72 crucial for understanding geodynamic behavior, as the presence of fluids dramatically reduces
73 viscosity thereby altering rheology [e.g., *De Meer et al.*, 2002; *Rosenberg and Handy*, 2005].
74 The magnetotelluric method (MT), which makes use of naturally-occurring external magnetic
75 fields and their induced electric currents within the Earth, is particularly useful in determining
76 the presence and distribution of fluids to substantial depths within the lithosphere [e.g., *Jones*,
77 1992; *Wannamaker et al.*, 2009]. In addition, viscosity and electrical conductivity are
78 suggested to be intimately related at the grain scale [e.g., *Tozer*, 1979].

79 Project phases INDEPTH-II (1994-95) and -III (1998-2001) collected MT data along
80 six separate profiles totaling 1600 km (Figure 1), that revealed the existence of anomalously
81 high electrical conductivity in the middle-to-lower crust across the entire region from the
82 Himalaya to the Kunlun mountains [*Wei et al.*, 2001]. These high conductivities, like those

83 interpreted from the earlier isolated MT measurements in southern Tibet (Figure 2) [*Pham et*
84 *al., 1986*], have been interpreted to represent partial melting in the crust, with the possible
85 presence of accompanying hydrothermal fluids [*Nelson et al., 1996; Chen et al., 1996; Wei et*
86 *al., 2001; Li et al., 2003; Bai et al., 2010; Rippe and Unsworth, 2010; Le Pape et al., 2012*].
87 The INDEPTH interpretations of a partially molten mid-crust in Tibet, initially reported in
88 *Nelson et al. [1996]*, have galvanized a whole generation of geodynamic modelers.

89 In 1995 broadband (BBMT) and long-period (LMT) MT data (together, coverage of
90 100 Hz–10,000 s) were acquired along our NNE-trending ‘100-line’ (Figure 2) crossing the
91 YZS at ~90 °E [*Chen et al., 1996*]. In 2001, approximately 200 km to the east along strike, MT
92 data were acquired along a new ‘700-line’ N-S profile crossing the YZS at ~92 °E [*Spratt et*
93 *al., 2005*] (Figure 2). Smoothed regional-scale models of these and other MT profiles further
94 west crossing the YZS were taken to show remarkable along-strike continuity of large-scale
95 conductivity structures from 77 °E to 92 °E, a distance of some 1,500 km [*Unsworth et al.,*
96 *2005*] (Figures 3c, 4a), attesting to the similarity of collisional processes along the whole
97 length of the suture zone.

98 This present paper compares and interprets new, high-resolution conductivity models
99 along the 700-line and 100-line profiles (Figures 1, 2), developed from re-analyses and re-
100 modeling of the data, and thereby provides strong constraints on viable tectonic models of this
101 region. We confirm, in greater detail than previously shown, the along-strike similarity of
102 crustal conductivity structures in southern Tibet. Contrary to prior smoothed models, we
103 highlight important cross-strike variations in conductivity that result from structural and
104 compositional changes, and differences in the amount and types of fluids within the crust.

105 **2. Geological background**

106 The Himalayan orogen, initiated by continental collision between India and Asia at ~57
107 Ma [e.g., *Leech et al., 2005*], conjoins the well-known tectonostratigraphy of the Sub-
108 Himalaya, Lesser Himalaya, Greater Himalaya (GHS) and Tethyan Himalaya. These zones are
109 separated respectively by the Main Boundary Thrust (MBT), Main Central Thrust (MCT) and
110 South Tibetan Detachment (STD), and together lie between the Main Frontal Thrust (MFT)
111 and the YZS [e.g., *Yin, 2006*] (Figure 1). The YZS separates the Himalayan terranes from the
112 Lhasa block that had earlier amalgamated with Asia prior to the collision of India [*Yin, 2006*].

113 The southern ends of our 100- and 700-lines lie above the Greater Himalayan
114 assemblage of ortho- and para-gneisses derived from a Neoproterozoic to Paleozoic passive
115 margin deformed and intruded during early Paleozoic thrusting onto the Indian margin, and
116 further deformed and intruded by leucogranites during Himalayan orogeny [*Yin, 2006*].
117 Located on the northern rim of the Himalaya range, the South Tibetan Detachment (STD) is a
118 low-angle, east-west trending, north-south extending, normal fault system (Figure 1b)
119 separating the Greater Himalaya from the Tethyan Himalaya [*Yin et al., 2006*]. Although the
120 Himalayan thrust faults are all presumed to sole into a single Main Himalayan Thrust (MHT),
121 along which India is currently underthrusting southern Tibet (Figure 1) [*Zhao et al., 1993*], it is
122 unclear whether the STD also soles into the MHT forming a wedge from which the GHS
123 undergoes ductile extrusion [*Grujic et al., 1996*], or whether the STD becomes the roof fault of
124 an extruding channel permitting middle- and lower-crustal flow outwards from beneath Tibet
125 [*Nelson et al., 1996; Beaumont et al., 2004*].

126 The Tethyan Himalaya are the largely unmetamorphosed Paleozoic-Mesozoic rift and
127 passive margin sequence deposited on the Indian continental margin; in the region of our

128 profiles they are dominantly Mesozoic clastics and carbonates [*Pan et al.*, 2004; *Antolín et al.*,
129 2011]. Windows within the Tethyan sequence expose the North Himalayan Gneiss Domes,
130 including the Kangmar dome [*Lee et al.*, 2000] (KD on Figure 2) crossed by our 100-line and
131 the Yalaxiangbo or Yadoi dome [*Zeng et al.*, 2011] (YXD on Figure 2) crossed by our 700-
132 line. The better-known Kangmar dome has been interpreted variously as a metamorphic core
133 complex [*Chen et al.*, 1990], as an antiform formed above a large ramp in, or duplex above, the
134 MHT [*Hauck et al.*, 1998], as due to duplex development along a north-vergent backthrust
135 system [*Makovsky et al.*, 1999], or as upwelling of a ductile mid-crustal channel being
136 extruded from beneath the Tibetan plateau [*Beaumont et al.*, 2004]. The Yalaxiangbo dome
137 and the Renbu (or Ramba) dome (RD on Figure 2) [*Guo et al.*, 2008] are both intruded by
138 leucogranites; published ages are 43–35 Ma in the former [*Zeng et al.*, 2011] and 11–7 Ma in
139 the latter [*Leech, 2008*].

140 The Tethyan Himalaya are separated from the Lhasa block by the ophiolitic mélanges
141 of the Yarlung-Zangbo Suture zone (YZS) (also termed the Indus-Zangbo suture zone and
142 Indus-Yarlung Tsangpo suture zone [*Meyerhoff et al.* [1986]) between India and Asia that
143 extends discontinuously for ~1,500 km along the Yarlung River valley [*Yin, 2006*]. The YZS is
144 bounded to the north by the south-vergent Gangdese thrust (GT), and to the south by the north-
145 vergent and younger Renbu-Zedong (RZT) or Great Counter Thrust [*Yin et al.*, 1994, 1999]
146 (Figure 2). The RZT and the STD were active coevally in the Miocene and may be
147 kinematically linked [*Yin et al.*, 1999]. The Lhasa block (or Lhasa terrane) to the north of the
148 YZS has a late Precambrian to Cambrian basement overlain by Paleozoic and Mesozoic
149 sedimentary rocks, but in its southern part is intruded by, and consists primarily of, the
150 Cretaceous-to-Eocene Andean-type Gangdese batholith and Linzizong volcanics that formed

151 during the northward subduction of the Tethyan ocean beneath Asia [*Kapp et al.*, 2007].

152 Consequent upon crustal thickening during the collision process, minor N-S diking and
153 associated east-west extension initiated by the mid-Miocene, ~18 Ma [*Yin et al.*, 1994], and
154 date termination of N-S thrusting on the RZT. Among the youngest features of the Plateau are
155 the still active north-south trending extensional grabens, such as the well-known Yadong-Gulu
156 rift in which our 100-line was located, and the discontinuous alignment of normal faults (Coma,
157 or Sangri-Cuona, rift) along which the southern part of our 700-line is located [*Armijo et al.*,
158 1986]. Significant geothermal activity exists, often within these graben systems, including a
159 prominent cluster in the Coma rift around stations 738–745 [*Hou & Li*, 2004].

160 Southern Tibet is becoming known as a major metallogenic province [*Hou and Cook*,
161 2009]. The Tethyan Himalaya in the area of Figure 2 contain more than 20 known mineral
162 deposits, notably Sb-Au and Ag-Pb-Zn ore bodies between the Lhunze Thrust and the STD [*Qi*
163 *et al.*, 2008]. A prominent cluster of such deposits (Mazhala–Zhaxikang) spans about 30 km
164 centered on station 740. The exposed mineralization results from middle to late Miocene
165 geothermal systems driven by leucogranite intrusion, with regional structural control by the
166 STD and the north-south normal fault systems [*Hou & Cook*, 2009; *Yang et al.*, 2009]. North
167 of the YZS the Gangdese belt also contains more than 20 mineral deposits of Cu-Mo porphyry
168 and Cu-Ar and Pb-Zn skarn deposits in the area of Figure 2 [*Li et al.*, 2006; *Hou et al.*, 2009].
169 The skarns formed at 30–20 Ma associated with calc-alkaline intrusions [*Li et al.*, 2006] and
170 the porphyries at 11–17 Ma associated with monzonitic stocks in turn related to deep-crustal
171 (adakitic) and upper-mantle (ultra-potassic) melts [*Hou et al.*, 2009]. Although these deposits
172 occur across a wide area, the Liangguchu and Shuangbujiere skarn deposits occur within 3 km
173 of stations 769 and 770 [*Li et al.*, 2006]. The Bairong Cu-Mo sulfide deposit is about 20 km

174 east of station 185 [*Hou et al.*, 2009].

175 **3. Geodynamic models and deformation of the Tibetan Plateau**

176 Currently popular hypotheses for the deformation of Tibet are that the entire lithosphere
177 deforms homogeneously ('vertical coherent deformation') as a thin viscous sheet [e.g.,
178 *England and Houseman*, 1986; *Flesch et al.*, 2005], or that deformation is dominated by a
179 more rapid ductile flow in the middle and/or lower crust above a stronger upper mantle
180 ('channel flow') [e.g., *Zhao and Morgan* 1987; *Shen et al.*, 2001; *Beaumont et al.*, 2004].
181 Many seismic and magnetotelluric experiments within Tibet provide proxies for lithospheric
182 temperature and evidence of crustal fluids, and inferred vertical strength profiles all have
183 minima in the crust, thereby permitting, though not requiring, channelized flow at the present
184 day [*Klemperer*, 2006].

185 The sparse Sino-French heat-flow [*Francheteau et al.*, 1984] and electrical conductivity
186 [*Pham et al.*, 1986] data, collected in the early 1980s between the locations of our 100- and
187 700-lines (Figure 2), provided initial evidence for partial melt within the upper crust of
188 southern Tibet. INDEPTH seismic reflection data north of the YZS identified "bright spots"
189 within the Yadong-Gulu rift interpreted as localized melt bodies [*Brown et al.*, 1996], or
190 aqueous fluids that would in turn trigger melting in the hot Tibetan crust [*Makovsky and*
191 *Klemperer*, 1999]. INDEPTH MT data recognized high conductivities associated with these
192 seismic bright spots, but showed that anomalously high conductivity was also present beyond
193 the confines of the rift, and continues to deep crustal depths in the Lhasa block [*Chen et al.*,
194 1996; *Li et al.*, 2003]. Inversions of INDEPTH passive seismic data (receiver functions and
195 surface waves) show that wave-speeds are abnormally low in the middle and lower crust of the

196 Lhasa block, but that the low-velocity zone is greatly reduced, and shallower, south of the YZS
197 [*Kind et al.*, 1996]. These data-sets were used to infer widespread melting of middle-lower
198 crust of the Lhasa block and its extrusion as the Greater Himalaya and Northern Himalayan
199 gneiss domes [*Nelson et al.*, 1996], an interpretation subsequently formalized in “channel-
200 flow” models [*Beaumont et al.* 2004, 2006; *Jamieson et al.*, 2004, 2006].

201 Temperature estimates for the upper-middle crust, at approximately 20 km depth
202 beneath the southern Tibetan Plateau, range from ~400–700°C [*Francheteau et al.*, 1984;
203 *Henry et al.*, 1997; *Alsdorf and Nelson*, 1999; *Beaumont et al.*, 2004]. Although these
204 temperature estimates are too low for dry melting, the presence of water that lowers the solidus
205 is suggested by the seismic and MT data [*Makovsky and Klemperer*, 1999; *Li et al.*, 2003].
206 Whether such melting is temporally and spatially ubiquitous, albeit at low melt fraction, or
207 whether it is patchy, will exert important controls on the deformation style of the crust. Initial
208 attempts (including our own) to generalize localized seismic and MT observations into regional
209 models [*Nelson et al.*, 1996; *Beaumont et al.*, 2004; *Unsworth et al.*, 2005] are being
210 challenged by newer, more spatially extensive datasets that suggest melting may be a
211 discontinuous phenomenon [*Hetényi et al.*, 2011; *Le Pape et al.*, 2012; *this paper*].

212 **4. Magnetotelluric method**

213 Common causes for high electrical conductivity in the Earth’s crust include graphite or
214 carbon films, fluids (either aqueous fluid or partial melt), interconnected metallic minerals, or
215 any combination of these [e.g., *Jones*, 1992; *Duba et al.*, 1994; *Bedrosian*, 2007].
216 Distinguishing between these causes requires additional geophysical, geochemical, petrological
217 and/or geological observations. Laboratory measurements [*Partzsch et al.*, 2000] show a strong

218 increase in electrical conductivity, ~ 1.5 orders of magnitude, over a narrow temperature
219 interval due to an increase of partial melt (to $>15\%$) to form an interconnected fluid network.
220 Quenching studies showed that the partial melt connected efficiently at low melt fractions (2%)
221 even on laboratory time scales [*Partzsch et al.*, 2000]. The electrical conductivity of partial
222 melts is dependent on the type of melt, the amount of fluid present and its connectivity [e.g.,
223 *Pommier et al.*, 2010; *Pommier and Le-Trong*, 2011]. The MT method is sensitive to this
224 dramatic increase in electrical conductivity, and has proven to be particularly useful in
225 identifying regions of partial melt associated with active orogenesis [e.g., *Schilling et al.*,
226 1997].

227 The magnetotelluric (MT) method provides information on the present-day, in-situ
228 electrical conductivity of the subsurface by measuring natural time-varying electromagnetic
229 fields at the Earth's surface [e.g., *Jones*, 1992; *Bedrosian*, 2007; *Chave and Jones*, 2012].
230 Electric currents in the Earth (telluric currents) are induced by natural time variations in the
231 Earth's magnetic field, driven by distant thunderstorms and solar winds. These electric
232 currents, in turn, produce time-varying (induced) secondary electric and magnetic fields.

233 The MT method involves comparison of the horizontal components of the total electric
234 (**E**) and magnetic (**H**) fields of the Earth, measured at the surface. These are related to each
235 other by a 2x2 complex impedance tensor (**Z**) that varies as a function of frequency and
236 position of observation [e.g., *Jones*, 1992; *Bedrosian*, 2007; *Chave and Jones*, 2012]. MT
237 response curves (amplitudes and phase lags with varying frequency) are calculated from the
238 mutually perpendicular electric and magnetic fields at each station. The vertical magnetic field
239 is also recorded and is related to the horizontal magnetic components by the geomagnetic
240 transfer function (TF). With increasing depth there is an exponential decrease in the amplitudes

241 of these fields. The depth of penetration, or ‘skin depth’, at which the amplitude of the fields
242 reduces to a factor of $1/e$ of that at the surface, increases at lower frequencies and in more
243 resistive rocks [e.g., *Jones, 1992; Bedrosian, 2007*].

244 The MT tensor is typically analyzed to determine the regional geoelectric strike
245 direction as well as the degree of dimensionality [e.g., *Jones and Groom, 1993*]. Within a two-
246 dimensional (2-D) Earth (in which conductivity structure varies laterally so that the apparent
247 resistivity is different along and across geologic strike), the impedances need to be calculated
248 in both directions (or modes) [e.g., *Jones, 1992; Bedrosian, 2007*]. Maxwell’s equations
249 formally decouple into two separate and independent modes. The transverse-electric (TE)
250 mode describes current flowing parallel to geoelectric strike, and is predominantly sensitive to
251 current concentration and flow patterns. The transverse-magnetic (TM) mode, on the other
252 hand, describes current flow perpendicular to strike, and is dominantly sensitive to charges
253 induced on conductivity gradients, and hence has very high lateral sensitivity. The vertical
254 magnetic mode transfer function, TF, which is only present in the TE mode case, senses
255 anomalous current flow in multi-dimensional structures; it is inherently insensitive to layered
256 strata of uniform conductivity.

257 In a 2-D Earth, tensor estimates from TE, TM and TF can be modeled together or
258 independently using forward and inverse modeling to provide estimates of subsurface
259 resistivity structures. Inversions of only the TM-mode data result in models that identify lateral
260 boundaries, as the TM-mode is primarily sensitive to charge accumulation on lateral
261 conductivity gradients. The TE-mode data are more sensitive to current flow, so to the
262 conductance of structures, identifying the depth to conductive zones, and thin sub-vertical
263 high-conductivity units. The vertical-field transfer functions (TF), typically displayed as

264 induction vectors with the real vectors reversed to point towards current concentrations in the
265 Earth (so-called Parkinson convention and adopted by international convention, *Hobbs*, 1992),
266 identify conductors, particularly at greater depths. Combined inversion of the TE-mode, TM-
267 mode, and TF-data shows a more complex, but more accurate, image of the true electrical
268 conductivity structure beneath a profile. These combined inversions are formally joint
269 inversions, in that trade-offs are often made – albeit in many cases by the inversion code, and
270 “hidden” from the user – between the various modes and data.

271 **5. Previous MT models: 100-line, 700-line and Sino-French data**

272 In the early 1980s, eight isolated MT soundings in the period range 0.001–1000 s were
273 carried out along a north-south-trending, 200-km-long profile crossing the Yarlung-Zangbo
274 Suture zone [*Pham et al.*, 1986] (stations T1-T8 in Figure 2). Stations north of the YZS
275 discovered remarkably low resistivities, $\sim 3 \Omega\text{m}$, within the depth range $\sim 12\text{--}33$ km. The
276 location of these high conductivities within the Himalayan geothermal belt was taken to imply
277 partial melts at depth [*Pham et al.*, 1986]. Two stations in the Tethyan Himalaya (T3 and T4 in
278 Figure 2), at about the latitude of the North Himalayan gneiss domes and where high heat flow
279 implies a shallow Quaternary intrusion [*Francheteau et al.*, 1984], found a similarly low
280 resistivity layer in the TE mode, from $\sim 3\text{--}14$ km depth, that was strongly anisotropic and much
281 more resistive in the TM mode [*Pham et al.*, 1986]. The single station at the southern margin
282 of the Tethyan Himalaya (T2 in Figure 2) did not observe unusually low resistivities [*Pham et*
283 *al.*, 1986].

284 The INDEPTH group made the first closely-spaced, broader-band recordings in 1995,
285 (our 100-line, stations 101 to 195 on Figure 2), along the Yadong-Gulu rift, across the

286 Kangmar Dome and the YZS, terminating in the southern part of the Yangbajain graben
287 (Figure 2). This profile consisted of 28 stations at ~10 km spacing, and recorded data in the
288 period ranges of 0.001–30,000 s [*Chen et al.*, 1996], although the range of interpretable quality
289 data is typically only 0.01–3,000 s (acquisition took place during the sunspot minimum
290 between Sunspot Cycles 22 and 23, so the longer period data are of poor quality). The 100-line
291 profile data have been modeled using several different approaches (Figure 3). *Chen et al.*
292 [1996] inverted both 2-D MT modes (TE+TM) and vertical field transfer function (TF) data
293 (Figure 3a). *Wei et al.* [2001] derived models from the TM-mode only (Figure 3b), and
294 *Unsworth et al.* [2005] derived smooth models using the TM-mode phase only and the TF data
295 (Figure 3c). Herein we model re-analyzed and corrected data using the apparent resistivities
296 and phases from both TM and TE modes (Figure 3d), showing derived phase differences
297 (discussed below) between the model and the data in Figures 3e (TE mode) and 3f (TM mode).

298 When considering how well a model fits MT observations, phase is used in preference
299 to resistivity. Residual effects of static shifts of apparent-resistivity curves are often present,
300 and would yield an expression of systematic bias at individual sites. Given modern MT
301 systems, very good data can be modeled to within 1°. For poorer quality data taken in difficult
302 terranes, or those with strong distortion, then the phases should typically be within 5°. Very
303 poor data have phase misfits in excess of 15°, and those models should be seriously questioned.
304 In our case, the majority of the data misfits are <5°, meaning that the major features are robust
305 and irrespective of data choice, inversion parameter choice, etc. The geometry and
306 conductivity of finer features may vary significantly with such choices, but here we focus on
307 the first-order features.

308 All of the published models show resistive material at the southern end of the profile,
309 but increasing conductivity further north (resistivities $<200 \Omega\text{m}$ below depths of 10–20 km),
310 starting ~150 km south of the YZS (Figure 3). Directly beneath or north of the YZS the crust
311 becomes extremely conductive at depth with resistivities $<30 \Omega\text{m}$, interpreted as partial
312 melting in the crust [Chen *et al.*, 1996; Nelson, *et al.*, 1996]. Because of the extreme
313 conductivity of the crust, low sunspot activity, and the limited bandwidth recorded, the 1995
314 data (100-line) were not able to characterize clearly the conductivity structure of the deepest
315 crust and uppermost mantle beneath the top of the high conductivity zone north of the Yarlung-
316 Zangbo Suture.

317 The 300-km-long 700-line profile comprises 28 broadband MT sites (BBMT) at
318 nominal 10 km spacing, and 15 long period sites (LMT) collocated with alternate BBMT sites
319 for a total period range of 0.004–30,000s (Figure 2). This profile was designed to augment the
320 100-line profile and also obtain to higher quality data at longer periods through extended
321 acquisition at selected sites. Unsworth *et al.* [2005] modeled the 700-line data using the TM-
322 mode phases and TF data (Figure 4a), excluding the TM-mode apparent resistivities and the
323 TE-mode data altogether, as part of a regional analysis of the entire Himalaya. Their model for
324 the 700-line profile shows strong similarities to the structures along the 100-line profile. They
325 interpret the high conductivity zone as saline fluids and partial melts interconnected beneath
326 the YZS. Our new model (Figure 4b), based on TM and TE data, provides significantly higher
327 spatial resolution allowing us to recognize geologically significant variability within the
328 continuous conductor modeled by Unsworth *et al.* [2005].

329 **6. New data modeling, 100-line and 700-line**

330 We derived and interpret new models for re-analyzed and corrected data from both the
331 100 and 700-lines (Figures 3d and 4b), and compare and contrast them with the previously-
332 published models (Figures 3 a,b,c and 4a). In order to determine the 2-D conductivity structure
333 of the region, regional MT data are modeled using a linearized, iterative inversion code. Such
334 solutions are non-unique and many of the features exhibited need to be tested or appraised to
335 determine how sensitive or robust they are to the measured data using both linearized [e.g.,
336 *Schwalenberg et al.*, 2002] and non-linearized [e.g., *Ledo et al.*, 2004; *Solon et al.*, 2005]
337 approaches.

338 Modern robust methods, and analyses for internal consistency, distortion,
339 dimensionality and strike [*Spratt et al.*, 2005] were used to obtain new regional 2-D responses
340 for the 100 and 700-line stations from 0.001 to 10,000 s. These data were analyzed for galvanic
341 distortion and dimensionality using the *McNeice and Jones* (2001) decomposition codes, then
342 the data were checked for internal consistency and inconsistent data removed [*Parker and*
343 *Booker*, 1996], a step not practised in developing the prior models. It was determined that a 2-
344 D model could validly represent the data at geoelectric strike angles of 108° (700-line) [*Spratt*
345 *et al.*, 2005], and 95° (100-line), with adopted error floors of 7% or greater. (The error floor is
346 the level below which errors are reset to that level. Errors that are larger than the error floor are
347 not affected. Parametric error estimates are often too small, as basic assumptions have been
348 violated. *Chave and Jones* [1997] demonstrate that jackknife estimates are far superior to
349 parametric estimates. Herein, most errors were derived using parametric methods. Poorly
350 estimated errors, either too low or too high, will yield biasing in the model. To correct for this,
351 an error floor is set. In this case, the error floor of 7% means an error floor of 7% in apparent

352 resistivities, and 2° in phase.) The distortion-corrected, 2-D regional MT responses were
353 modeled using several combinations of data and model parameters in order to thoroughly
354 explore model space for the 2-D structure of the region [see *Spratt et al.*, 2005]. Modeling was
355 undertaken using *Rodi and Mackie's* [2001] RLM2DI inversion algorithm, as implemented in
356 Geosystem's WinGLink interpretation software package. This code searches iteratively for the
357 smallest RMS (root mean squared) misfit, while simultaneously attempting to trade off the fit
358 to the observed data (data misfit) with model roughness. The models found represent minimum
359 structure required to fit the data with an acceptable misfit.

360 The inversion runs were initiated with a uniform half-space of $200 \Omega\text{m}$ and a mesh
361 consisting of columns with minimum 2 km width, increasing at the model edges (74 columns
362 for the 700-line, 91 for the 100-line), and rows increasing from 500 m thick at the surface to
363 2.5 km thick at 40 km (700-line, 51 rows) and from 300 m to 3 km (100-line, 45 rows). The
364 error floors, determined from the acceptable misfit values obtained in the distortion analysis,
365 were set to 7%, equivalent to a 2° error in the phases. The resistivities were set with a higher
366 error floor of 20% to account for residual static shift or site gain effects, since these were
367 expected to be small [*Groom and Bailey*, 1989]. The tradeoff between data misfit and model
368 smoothness is controlled by the regularization parameter τ , where a low value results in a
369 closer fit to the actual data but a rough model, and a high value sacrifices fit for smoothness.
370 After running several models from a uniform half-space using various values of τ , it was
371 determined that a value of 3 resulted in the smoothest models with acceptable fits to the data
372 (lowest RMS value). Many 100s of iterations were run to obtain each final model, in order to
373 be sure we reached the minimum misfit value obtainable by the data. Several of the modeling
374 parameters (including the option to invert for static shift), as well as the conductivity values of

375 some features, were adjusted between model iterations, where the program was stopped,
376 altered and restarted, in order to observe the effects of the changes and to reach the most
377 appropriate final models with an acceptable misfit value.

378 Inversions were run using the TM data alone, the TM and TF data together, the TM and
379 TE data together, and, finally, the TM, TE, and TF data. The models of differing data
380 components (TM-only, TM+TE, and TM+TE+TF) demonstrate that the general electrical
381 structure along the length of the profile is consistent throughout the data, although the shape
382 and depth of the different features vary marginally between models [*Spratt et al.*, 2005]. The
383 RMS misfit value for each model was reduced for the 700-line from 15.9 for a uniform half-
384 space to 1.8 for the TM-only data, 2.9 for the TE and TM data and 4.1 for the TM, TE and TF
385 data; and for the 100-line from 10.5 for a uniform half-space to 2.6 for the TM-only data, 2.8
386 for the TE and TM data and 4.6 for the TM, TE and TF data. The TM data alone were
387 sufficient to capture important regional details, but the TM+TE model that also has a
388 reasonable misfit value appears to result in a higher resolution of thin near-vertical features that
389 do not appear in the TM-only models. The TM+TE models were therefore used for further
390 analysis and along-strike comparison (Figures 3d, 4b).

391 The measured and calculated phase differences of both the TM and TE data (Figures 3
392 e,f and 4 c,d) show a generally good fit ($< \pm 5^\circ$ for most periods at most sites) over the entire
393 frequency range. This, together with the consistencies between models utilizing different data
394 components, different approaches to static shifts, and different satisfactory misfit values,
395 indicates that the main model features are robust irrespective of the data used or the inversion
396 parameters.

397 **6.1 Hypothesis Testing**

398 There exists a uniqueness theorem for perfect continuous MT data over a 1-D Earth
399 [*Bailey, 1970*], but MT models are inherently non-unique due to data insufficiency, inadequacy
400 and inaccuracy. Linearized model appraisal is useful, but is notoriously imprecise in highly
401 non-linear methods such as EM [e.g., *Ledo et al., 2004; Solon et al., 2005*]. Thus, forward
402 modeling is required to verify model features and to determine model sensitivity. Hypothesis
403 testing involves altering the conductivity values of individual cells in the final model and
404 forward calculating the MT responses of the altered model for each site. Pseudosections
405 showing the difference between the original responses and those from the altered model allows
406 a comparison between the apparent resistivities and phases calculated from the original and
407 altered models. This technique was applied to key features in the final models shown in
408 Figures 3d for the 100-line and 4b for the 700-line.

409 Conductor C, at the northern end of both profiles, was replaced with a resistive block
410 below 60 km depth on the 700-line, to determine the depth of penetration beneath this region
411 (Figure 5a). Phase difference plots between calculated responses of the original versus the
412 altered model show no significant differences in either the TM- or TE-mode data (Figure 5a).
413 This demonstrates that our data were unable to penetrate the high conductivity of C below 60
414 km, and are insensitive to the deep crust north of the YZS, consistent with the 100-line model
415 of *Chen et al. [1996]* (Figure 3a). We mark the corresponding area of our final model as a
416 “zone of no penetration” (Figure 9b).

417 To test the existence of resistor D that separates mid-crustal conductors B and C, the
418 two conductors were connected on the 700-line (Figure 5b), removing the gap between the two
419 and forming one long conductor, as suggested in the modeling by *Unsworth et al. [2005]*

420 (Figure 4a). The overall RMS misfit of the altered model is increased from 2.8 to 4.2, and
421 phase difference plots between the responses calculated from the original model versus the
422 altered model show distinct differences $> \pm 10^\circ$ (Figure 5b), indicating that the resistive break is
423 required by the data. The response to the break is predominantly observed in the TM data and
424 is due to the sensitivity to charges on the boundaries between the conductors and the resistive
425 region that are absent when the two conductors are connected. In contrast, the TE data are
426 sensitive to the geometry of current distribution, and the difference in current flow between the
427 two models is minor and below our ability to detect (phase differences $< \pm 5^\circ$, Figure 5b TE
428 mode).

429 To further analyze the shape and extent of resistor D, we increased the resistivity below
430 conductors A and B on the 700-line to match the resistivity observed within feature D (Figure
431 5c). The RMS of the altered model barely changes from the original model, and phase
432 difference plots do not reveal significant differences in either the TE- or TM-modes. Hence the
433 intermediate resistivity values beneath ~ 30 km depth below features A and B in the 700-line
434 model could be a shadowing effect of these shallower high-conductivity features, and the true
435 resistivity values could be similar to those observed within feature D. Hypothesis testing (not
436 shown) modifying the region below B to a depth of 100 km to be either highly conducting
437 (700Bcond: $1 \Omega\text{m}$) or highly resistive (700Bres: $10,000 \Omega\text{m}$) and inspecting the difference
438 between the forward responses of the two models (700Bres-700Bcond) shows that there is
439 almost no sensitivity in the TE mode to the region below B, but detectable sensitivity at some
440 sites in the TM mode (approx. $\pm 6^\circ$). This is because in the TE mode the currents flowing in B
441 mask the geometry of currents flowing below it, whereas in the TM mode there is a significant
442 difference in the geometry of charges on conductivity boundaries that result in observable

443 responses. Using either 700Bcond or 700Bres as the start model, and finding the closest
444 acceptable model to it when inverting, yields models that give the minimum and maximum
445 permitted resistivity below B, which are 10 Ωm and 1,000 Ωm respectively. We thus mark the
446 corresponding area of our final model (Figure 9b) as a “zone of poor resolution”.

447 Similarly, along the 100-line profile, feature D was tested by altering conductivity
448 values in three different ways (Figure 6). We replaced the conductor linking feature C to the
449 surface with a resistor linking D and E (Figure 6a); we connected conductors B and C with a
450 conductor that cut across resistor D (Figure 6b, analogous to Figure 5b for 700-line); and we
451 moved the upward continuation of conductor C to the surface, south of the YSZ and again
452 cutting across resistor D (Figure 6c). In each case the RMS value of the forward inversion
453 increased significantly from the original model, from 2.8 to 3.5, 3.9 and 4.7, respectively, and
454 the phase differences between the original and altered models was $>15^\circ$ beneath feature D in
455 the TM-mode.

456 We conclude that resistive zone D separating conductors B and C on both profiles is
457 required by the data and is not an artifact of our modeling methodology. Indeed, the
458 smoothness criterion in the objective function is trying to connect the two conductors, as that
459 would result in a lower total roughness, but the misfit component of the objective function
460 works against this and requires D to exist in order to minimize the misfit.

461 Note that for both profiles, sensitivity to the existence of the resistive break is in the
462 TM-mode data, not the TE-mode data. Arguments about 3-D effects on 2-D interpretations can
463 be made about some TE-mode data features, but not about TM-mode data features as the TM-
464 mode is generally far less sensitive to 3-D structure [e.g., Jones, 1983; Wannamaker et al.,
465 1984; Ledo, 2005].

466 **6.2 Focused Models**

467 To better define upper-crustal structure, we undertook more detailed and focused
468 modeling by selecting only higher-frequency data, at periods in the range of 0.004 to 100 s,
469 from selected groups of stations with much finer modeling and inversion meshes. The resulting
470 focused models (Figures 7, 8) better represent the shallow structure because the responses of
471 local structures have a higher influence on the average misfit value, whereas our crustal-scale
472 models (Figures 3, 4) are smoothed because the modeling program is simultaneously fitting all
473 of the data along the profile and is able to misfit some local data structure (see, *Jones*, 1993,
474 for a discussion on this). This issue is particularly evident, for example, when comparing the
475 southern edge of conductor C that on the regional-scale models clearly extends up towards the
476 surface in the 700-line model, but not in the 100-line (Figures 3d, 4b), whereas the focused
477 models clearly show conductor C also reaching close to the surface on the 100-line (Figure 7c).
478 Where the focused models geographically overlap (Figure 7c with 7b, 8c with 8b, 8b with 8a)
479 the derived models differ because they are fitting different subsets of the data. The preferred
480 model is the central part of each focused model, away from edge effects.

481 **6.3 Geometric Description of Crustal and Focused Models**

482 The models generated for the 700-line and the 100-line profiles show remarkable
483 similarities. Five seemingly equivalent first-order features (conductive regions A, B, C and
484 resistive regions D and E) can be identified on both Figures 3d and 4b.

- 485 1. Feature A (100-line: Figures 3d, 7a; 700-line: Figures 4b, 8a) is a conductive region of
486 $\sim 1 \Omega\text{m}$, located near the southern end of the 700-line and 100-line profiles from near-
487 surface down to a depth of 5–10 km.

- 488 2. Feature B (Figures 7b, 8b) is a group of conductive zones, also of $\sim 1 \Omega\text{m}$, in the region
489 of the North Himalayan gneiss domes and always south of the YZS that spans a greater
490 depth range, down to $\sim 20\text{--}30$ km (although in general the base of conductors are poorly
491 defined).
- 492 3. Feature C is a northward-dipping conductor of $\sim 1 \Omega\text{m}$ that is located beneath and north
493 of the YZS. At the north end of both profiles beneath the Gangdese batholith
494 conductive region C is below $\sim 25\text{--}30$ km (Figures 3d, 4b), but closer to the suture it
495 trends upwards and becomes shallower than ~ 10 km at ~ 25 km south of the YZS (700-
496 line) or at ~ 10 km south of the YZS (100-line) (Figures 7c, 8c).
- 497 4. Feature D (Figures 3d, 7c, 4b, 8c) is a near-vertical resistive structure, of $\sim 2,000 \Omega\text{m}$
498 that clearly separates the mid-crustal conductors B and C. At the latitude of feature D,
499 the entire crustal thickness is resistive, except the very near surface.
- 500 5. Feature E (Figures 3d, 7c, 4b, 8c) is a highly resistive region ($>10,000 \Omega\text{m}$) that lies
501 directly above the large conductive region of feature C, extending from the surface in
502 the vicinity of the YZS, down to the top of C at >25 km depth.

503 The features in the 100-line and 700-line models were imaged using independent data
504 sets measured during separate field seasons, during different times in the solar cycle. The
505 similarities in the geometries and properties of the conductivity structures along the two
506 profiles are most simply interpreted as representing continuity along-strike. Such along-strike
507 continuity suggests that the observed conductivity patterns are regional and related to orogen-
508 scale processes, and requires consistent interpretations between the two profiles. There are of
509 course some more minor differences between the 700-line and 100-line results, presumably
510 due to local differences in shallow geological structure. For example, the detailed geometry of

511 the separate conductors forming B differs from the 100-line (Figure 7b) to the 700-line (Figure
512 8b), and B is somewhat shallower and of lower conductance on the 100-line. Conductor C is
513 connected to the surface on the 700-line (Figure 8c), but does not reach shallower than 5 km on
514 the 100-line (Figure 7c).

515 Perhaps the most important difference between our new models and those previously
516 published is the presence of feature D, the resistive region separating two conductive zones
517 (features B and C) located 10–30 km south of the YZS, evident on the regional models
518 (Figures 3d, 4b) and confirmed on the focused models (Figures 7c, 8c). This resistive structure
519 has strong implications for the extent, connection and distribution of fluids in the crust, hence
520 on the geodynamic processes active in Tibet. Compared to previous models, our new models,
521 from re-analyzed and corrected data, use both the TM and TE-modes, use a finer mesh and
522 lower smoothing parameter, and fit the data better.

523 **7. Geological Interpretations of Conductors**

524 **7.1 Conductor A**

525 Conductor A at the southern end of both profiles is interpreted to represent aqueous
526 fluids within the Tethyan sedimentary sequence [*Spratt et al.* 2005]. The 100-line is in a region
527 where the generally east-west trend of the STD is disrupted by the NNE-trending Yadong-Gulu
528 rift (Figure 2). INDEPTH wide-angle seismic profiling along our 100-line shows that the
529 Neogene rift-related sediments are never thicker than 1 km [*Makovsky et al.*, 1996a] so clearly
530 lying above the highest conductivities. INDEPTH reflection profiling along the 100-line was
531 used to interpret the STD from surface outcrop to depth [*Hauck et al.*, 1998] (dashed line in
532 Figure 7a), bounding the base of the highest conductivities. The interpretation of conductor A

533 as meteoric or connate fluids in the Tethyan sedimentary rocks agrees well along the 700-line
534 profile where the base of the prominent conductor may mark the STD, the surface trace of
535 which is just south of station 710 but runs south-north just west of stations 710–720. In Figure
536 8a we show the structural interpretation of *Hauck et al.* [1998] translated 200 km east, fully
537 aware that in this location the surface outcrop of the STD runs approximately north-south
538 [*Long et al.*, 2011] and close to stations 710–720. The STD may be significantly shallower
539 than shown directly beneath these stations which, however, may be sensing the conductivity
540 structure of the sedimentary series deepening to the east of our profile. Both the 100- and 700-
541 lines show significant variability of conductivity within the Tethyan sedimentary series,
542 presumably due to fluid circulation driven by terrain-induced advective flow to depths of
543 several kilometers [*Hochstein & Yang*, 1992] in the Yadong-Gulu and Coma rifts respectively,
544 as attested to by the numerous hot and warm springs along the southern parts of our profiles
545 [*Hou and Li*, 2004] (Figure 9). Conductivity variability may also relate to the large range of
546 lithologies present (carbonates, slates, sandstones) [*Pan et al.*, 1994], and their different
547 porosities and permeabilities.

548 **7.2 Conductors B**

549 Moving northwards along the 100- and 700-lines, conductors B lie in a region where
550 the detailed shallow subsurface geometry is poorly known beneath the North Himalaya Gneiss
551 Domes on the 100-line (Kangmar dome), and essentially unknown on the 700-line
552 (Yalaxiangbo dome). Conductor B was previously interpreted by *Unsworth et al.* [2005] as a
553 continuous zone of ponded melt in the middle and upper crust connected to conductors A and
554 C, but in our more complete modeling it is discrete and appears far more complex. Comparison
555 with previously published cross-sections [*Lee et al.*, 2000] (Figure 7b) shows that our MT

556 measurements clearly image the resistive core of the Kangmar dome bounded by the STD that
557 separates highly resistive orthogneisses below from conductive Tethyan Himalaya sedimentary
558 rocks above. Both *Lee et al.* [2000] and *Makovsky et al.* [1999] suggest Tethyan Himalayan
559 rocks are also present at depth beneath the Kangmar dome, albeit carried along south-dipping
560 and north-dipping thrusts respectively. At 10–20 km depth, south-dipping reflections on
561 INDEPTH seismic data (projected from ~20 km east; dashed lines on Figure 7b) may represent
562 back thrusts carrying Tethyan sedimentary material [*Makovsky et al., 1999*], providing a
563 possible cause of somewhat elevated conductivities vertically beneath the Kangmar dome
564 (southern region labeled B in Figure 7b). However, the northern and more conductive segment
565 labeled B lies at the same depth as the bright spot of the “Yamdruk-Damxung reflection band”
566 imaged ~50 km due east on INDEPTH reflection data [*Brown et al., 1996; Hauck et al., 1998*]
567 (dashed oval on Figure 7b). This bright spot is close to Yamdrok Tso (Yamdruk lake) in which
568 *Francheteau et al.* [1984] measured heat flow of 146 mW/m² (Figure 2) and argued, from the
569 magnitude of the heat flow and the rapid spatial gradient in heat flow declining to the south,
570 that an anomalous heat source, presumably magmatic, intruded within the past 1 Ma at less
571 than ~10 km depth [*Jaupart et al., 1985*]. Two MT soundings close to the lake and the seismic
572 bright spot (Figure 2) were interpreted as showing resistivities as low as 3 Ωm in the 3–14 km
573 depth range [*Pham et al., 1986*], further corroborating the interpretation of a shallow magma
574 body. We therefore interpret at least the portions of conductor B at ~15 km depth and below as
575 including a magma body, though the observed resistivities are so low, ~1 Ωm, comparable with
576 the resistivity of felsic partial melt, that saline aqueous fluids that can have conductivities 100
577 times greater than felsic melts are likely also present [cf. *Li et al., 2003*]. The portion of
578 conductor B above 10 km (above the dotted line in Figure 7b), most prominent beneath stations

579 140 and 143, could be an apophyse of the deeper intrusion, or more probably meteoric or
580 connate waters in the Tethyan Himalayan sequence.

581 Separating magmatic and aqueous sources for conductor B on the 700-line is similarly
582 difficult. The portion of B that rises to the surface between stations 745 and 747 (Figure 8b) is
583 plausibly related to the hydrothermal system within the Tethyan Himalayan sequence that
584 drives the hot springs scattered between stations 740 and 747 [*Hou and Li, 2004*]. These
585 springs reach the surface south of the north-dipping Lhunze thrust (with its surface trace
586 between stations 745 and 747), and north-dipping conductor B may mark aqueous fluids rising
587 along, or trapped beneath, this thrust being potentially driven by a magmatic source at greater
588 depth. (The Lhunze thrust crosses our line of section obliquely (Figure 2) and in Figure 8b is
589 shown in its geometric position with respect to the MT stations, not to the line of section.)
590 Such fluxing fluids may also act as mineralizing agents, and their deposits can also be
591 conductive [e.g., *Livelybrooks et al., 1996*]. The Cuomei-Longzi belt [*Qi et al., 2008*], that
592 crosses the 700-line near station 740 with an alignment of Sb-Pb-Zn deposits, is likely to
593 contain numerous conductors and may contribute to the anomalies that we observe here and
594 elsewhere along the 100- and 700-lines. However, these potentially conductive ore bodies of
595 magmatic-tectonic origin (i.e. not strata-bound due to depositional origin) are small and
596 isolated by resistive country rock. Similar bodies elsewhere are not typically directly
597 observable using regional MT methods [e.g., *Livelybrooks et al., 1996; Heinson et al., 2006*]
598 except at the highest frequencies (10 Hz–10 kHz, so-called “audio-MT” or AMT [e.g., *Jones &*
599 *Garcia, 2003*]. Thus, if conductor B on the 700-line only represents mineralization, it would be
600 an extraordinary, world-class deposit. The more realistic dominant source for this conductor is
601 aqueous fluids.

602 The south-dipping northern portion of B that spans a depth range 20–10 km or even
603 shallower (Figures 8b and c), by analogy with our interpretations above of the 100-line (Figure
604 7b), could represent a magma body similar to that seismically imaged 100 km due west.
605 Although brines in Tethyan sedimentary rocks beneath the Yalaxiangbo dome are a possible
606 alternative, regional cross-sections across the Yalaxiangbo dome (admittedly less well-studied
607 than the Kangmar dome) do not show Tethyan sedimentary rocks beneath the dome [*Yin et al.*,
608 2010]. Although it is intriguing that the northern part of conductor B is shallowest beneath the
609 granitic core of the Yalaxiangbo dome, even if magmatic the conductor cannot be directly
610 related to the exposed granites, for which the youngest age yet reported is 35 Ma [*Zeng et al.*,
611 2011]. The exposed granites (stations 753, 755) do not appear particularly resistive; just as on
612 the 100-line, the most resistive lithologies appear to be the Cambrian orthogneiss (around
613 stations 749, 750, and 758) (Figure 8b).

614 **7.3 Conductor C**

615 Conductor C, northward-dipping beneath the YZS in both profiles, and below the
616 Gangdese batholith further north, is confidently interpreted as partial melt where the conductor
617 is in the mid-to-lower crust (Figure 9). This interpretation is based on many other geophysical
618 data that support the presence of partial melting in the Lhasa Block below 15 km depth,
619 including observations of seismic bright spots and shear-wave conversions close to the 100-
620 line (Figure 2), a shallow Curie isotherm derived from satellite magnetic data, high heat flow,
621 observations of a low seismic velocity zone, and interpretations of INDEPTH line-200 MT
622 data [*Klemperer, 2006, and refs. loc. cit.*]. The dashed lines in Figure 7c delineate a reflective
623 band, the “Yarlung Zangbo reflector” recognized on wide-angle seismic data by *Makovsky et*
624 *al.* [1999]. *Nelson et al.* [1996] presumed these reflections at ~20 km depth represented magma

625 bodies, even though the geometry of the seismic experiment did not allow observation of
626 shear-wave conversions capable of testing whether these reflections south of the YZS represent
627 fluids. In contrast, because upper-crustal attenuation of seismic shear waves decreases from
628 north-to-south across the suture [Makovsky *et al.*, 1996], and because the Yarlung Zangbo
629 reflector also deepens northwards, becoming deeper than the magmatic bright spots observed
630 close to station 195, Makovsky *et al.* [1999] suggested this reflective band was related to an
631 ophiolitic slab. However, ophiolites, even when serpentinized, are typically not conductive
632 because their magnetite is disseminated and not connected [e.g., Weckmann *et al.*, 2007]. The
633 geology is well-mapped along the 700-line where opposing thrust systems (Gangdese thrust and
634 Renbu-Zedong thrust) bound the YZS, here a *mélange* of ophiolitic and sedimentary material
635 [Yin *et al.*, 1994, 1999], and it is clear that the ophiolitic *mélange* has high resistivity (around
636 station 769) (Figure 8c).

637 In the Lhasa Block the tops of the seismic bright spots appear to represent saline fluids
638 released from, and accumulating above, cooling magma bodies [Makovsky & Klemperer,
639 1999], an interpretation consistent with the coincident MT observations [Li *et al.*, 2003].
640 Hence we infer magmatic and/or aqueous fluids migrating upwards through the brittle crust
641 may be the origin of the fingers of high conductivity projecting upwards immediately south of
642 the YZS on the 100-line and 700-line. Although the thrust geometries on Figure 8c must be
643 regarded as conjectural at even 5 km depth, where conductor C reaches the surface the highest
644 conductivities are presumably contained within the Tethyan series above the RZT. Station 764
645 is in Triassic turbidites [Antolin *et al.*, 2011], with no geothermal indicators reported within 40
646 km [Hou and Li, 2004], suggesting that the shallowest part of this anomaly is due to meteoric
647 or connate fluids, not to a very shallow magma body. Less structural data is available directly

648 across the YZS for the 100-line than for the 700-line, and the geometry of the RZT and GT
649 shown in Figure 7c from *Makovsky et al.* [1999] is only a cartoon. Nonetheless, the geometry
650 of the tongues of high conductivity (B and C in Figures 7c and 8c) approaching shallow depths
651 is not suggestive of solid-phase conductors dismembered by low-angle thrusting, and our
652 preferred interpretation of conductor C at ≥ 10 km depth is magma and associated brines. On
653 the 100-line where the highly-conductive tongue approaches the surface immediately south of
654 the YZS (Figure 7c), hot springs are known along the Yarlung River <20 km east of station
655 165, lending additional support to interpretation of the shallowest part of conductor C as young
656 intrusions and associated magmatic fluids.

657 **7.4 Resistor E**

658 The highly resistive feature E is shown in the MT model north of the Yarlung-Zangbo
659 suture to depths of the order of 20 km. This regional feature undoubtedly represents the
660 resistive Gangdese batholith of the Lhasa block (Figure 9). It is noteworthy that in this
661 metallogenic province there are numerous Cu-Au skarn and porphyry deposits, including some
662 within 3 km of stations 769 and 770 [*Li et al., 2006*]. There is no evidence in our MT data of
663 the effects of near-surface conductors related to these economic mineralized deposits, which
664 disinclines us to interpret other anomalies along our profiles as mineralized zones, even though
665 we cannot rule out this possibility.

666 **7.5 Resistor D**

667 Feature D on both profiles is a resistive unit ($\sim 2000 \Omega\text{m}$) south of the YZS that clearly
668 separates the two mid-crustal conductors B and C, as shown by our hypothesis testing (Figures
669 5b, 6b). Although the inferred resistivity of D is greater than that shown in our models for

670 Greater Himalayan material beneath the STD (Figures 7a, 8a), hypothesis testing (Figure 6c)
671 shows that we lack resolution to demonstrate that these regions have different resistivities.
672 Hence D, lying structurally beneath the Renbu-Zedong Thrust, is most simply interpreted as
673 Greater Himalayan basement. The gross similarity of the sequence conductor B–resistor D–
674 conductor C on both the 100- and 700-lines is striking; yet D is aligned with exposed ophiolites
675 on the 100-line (centered on station 160) but 20 km south of the ophiolite belt on the 700-line
676 (centered on station 762) (Figure 2). Our two profiles are separated by 200 km along-strike,
677 and have just a 20-km difference in cross-strike location of D with respect to the suture zone.
678 We could regard this 20-km difference as trivial, and infer that the upper-crustal portion of D
679 relates to the suturing process, in which case D could even represent YZS ophiolitic mélange
680 that we know is resistive in the shallow subsurface between the RZT and Gangdese thrust
681 (Figures 7c, 8c). Or we could regard this difference as representing post-suturing modifications
682 in conductivity geometry. Our interpretation of C as having a geologically recent magmatic
683 component implies C can cross-cut older structure, and suggests that the location of D is
684 simply a manifestation of the southern extent of recent intrusions propagating upward from the
685 major partial melt zone beneath the Gangdese batholith.

686 The existence of resistor D fundamentally distinguishes our new models from those of
687 *Unsworth et al.* [2005] in which the conductors C and B to the north and south of the YSZ are
688 electrically connected. We can place upper limits on how much fluid can be present within
689 resistor D [cf. *Keranen et al.*, 2009]. We estimate a high upper bound of <2.5% melt within
690 resistor D with the widely used modified Archie's Law [*Hermance*, 1979], that predicts weakly
691 interconnected hence large volumes of melt to achieve a specific conductivity, with a melt
692 resistivity of 1 Ωm and infinite matrix resistivity. However, if resistor D were deforming at the

693 present day we would expect melt to be interconnected along grain boundaries [*Jin et al.*,
694 1994], the upper Hashin-Shtrikman bound would apply, and melt content would be limited to
695 <0.1%, far too low to facilitate any deformation [*Rosenberg & Handy, 2005*]. Clearly, resistor
696 D is *not* a deforming partially molten zone, and we interpret it as a melt-absent region of the
697 orogen, in contrast to conductors B and C south and north of the YZS.

698 It is noteworthy that on the 100-line resistor D cuts vertically through the seismic wide-
699 angle “Yarlung Zangbo reflector” (YZR) of *Makovsky et al.* [1999] projected 50 km west from
700 its suggested location (Figure 7c). We do not see this as a conflict, as the data from the portion
701 of the YZR crossed by resistor D (dotted lines below 20 km in Figure 7c) are significantly less
702 clear than data further north or south. *Makovsky et al.* [1999] pointed to ambiguity of
703 identification of reflections in this location as due to interference from S waves. In contrast,
704 we suggest that the YZR is simply not continuous between the well-imaged segments further
705 south and further north (dashed lines below 20 km in Figure 7c). A search for analogous
706 reflectivity closer to the 100-line at the YZS successfully imaged the northern part of the YZR
707 but identified no comparable reflections close to our stations 155 and 160 [*Zhao et al., 1997*].

708 **8. Tectonic Implications**

709 Modern geodynamic models for Tibet all emphasize the importance of a weak middle-
710 lower crust capable of flow [e.g., *Zhao and Morgan, 1987; Shen et al., 2001; Beaumont et al.,*
711 *2004*] that is attested to by a wide range of geophysical data [summarized in *Klemperer, 2006*],
712 including our conductor C beneath and north of the YZS. A continuing debate is whether
713 boundary conditions at the edges of the Tibetan Plateau allow crust to flow beyond the Plateau
714 margins, in particular at the southern, Himalayan margin.

715 *Beaumont et al.* [2004] used coupled thermal-mechanical models to show how ductile
716 extrusion between the MHT and the STD (Figure 1), together with the effects of surface
717 denudation, can explain many geologic features observed in the Himalaya-Tibetan system, as
718 well as the INDEPTH geophysical observations [*Nelson et al.*, 1996] that were central to the
719 development of this “channel-flow” model. P-T-t transects across the Greater Himalaya have
720 been argued to support [e.g., *Jamieson et al.*, 2004] or repudiate [e.g., *Kohn*, 2008] channel-
721 flow extrusion of these rocks during the Miocene. Channel-flow that is active at the present-
722 day seems to require a melt-weakened channel that extends continuously from the
723 uncontroversial hot, weak middle-lower crust of the Lhasa and Qiangtang blocks, at least as far
724 south as the surface expression of the STD, and be in the upper crust, above the MHT. Such a
725 continuous zone of shallow melt extending north and south of the YZS has been proposed from
726 both MT [*Unsworth et al.*, 2005] and seismic [*Caldwell et al.*, 2009] data. Other higher-
727 resolution seismic data clearly show that the intensity of reflectivity anomalies is spatially
728 variable [*Brown et al.*, 1996; *Hetényi et al.*, 2011]. *Brown et al.* [1996] suggested the brightest
729 reflections are magma chambers within a laterally continuous reflector zone marking variably
730 molten and cooled intrusions, arguably the top of a weakened zone of channelized flow,
731 whereas *Hetényi et al.* [2011] argue that the absence of a pronounced upper-crustal low-
732 velocity zone beneath some of their seismic stations brings into question the mechanical
733 viability of the channel flow model, though they fail to show that lower degrees of partial melt
734 still consistent with melt weakening are not present.

735 Our results, modeling additional components of almost the same data that were used by
736 *Unsworth et al.* [2005] to infer a continuous low-resistivity layer from the Lhasa block to the
737 Tethyan Himalaya, are the first to show unequivocally that a melt-weakened layer is not

738 continuously present within the upper crust of southernmost Tibet. Our focused modeling in
739 the vicinity of the YZS (Figures 7c, 8c) shows a highly resistive block D from near-surface to
740 ≥ 25 km depth. Our hypothesis tests (Figures 5b, 6b) demonstrate that any conductor
741 breaching resistor D would yield unacceptable fits to the recorded data. Simple calculations
742 using appropriate resistivities for basement lithologies and crustal melts show that partial melt
743 within resistor D, if any, is limited to $\sim 1\%$ at most, and more realistically $\sim 0.1\%$. Thus on our
744 two separate transects separated by >200 km we have shown that a continuous partially melted
745 channel is not present.

746 Channel flow could still be operating today if the crust represented by resistor D is
747 sufficiently weak to flow even in the absence of melt. This we consider highly unlikely given
748 the high resistivity of resistor D of some $2,000 \Omega\text{m}$. Alternatively, channel flow could be
749 operating today if our transects are not representative, so that at other locations along strike
750 there is melt-weakened crust continuously present from north to south, perhaps in a complex
751 3D network at a kilometric scale, allowing for a complex channel structure. Such a situation
752 has recently been reported for melt progression north of the Kunlun Fault, where the MT data
753 yield unequivocal evidence for anisotropy [*Le Pape et al.*, 2012]. The observed electrical
754 anisotropy is interpreted by those authors as the manifestation of finger-like melt penetration in
755 contrast to pervasive melt penetration. If resistor D is related to the thrust geometry of the
756 suture zone and formed as a continuous block along strike, then we have no reason to expect
757 that cross-sections between the 100- and 700-lines would find substantially different structures.
758 If instead resistor D simply marks the southern limit of geologically recent intrusions
759 propagating upward from beneath the Lhasa block, then such intrusions might reach different
760 distances south of the suture at intervening locations. Indeed, preliminary MT profiling along-

761 strike along the YZS suggests a variability in conductivity west of the 100-line and east of the
762 700-line as dramatic as we observe across-strike on our profiles [Wei *et al.*, 2010]. Finally, we
763 note that in numerical thermo-mechanical models of channel flow in the India-Asia collision,
764 the distance which Indian crust underthrusts Asian crust north of the ISZ is sensitive to small
765 changes in crustal strength [Beaumont *et al.*, 2006]. For a range of models that all show
766 channel-flow, Indian crust may underthrust 200 km north of the YSZ or not underthrust at all
767 [Beaumont *et al.*, 2006; Jamieson *et al.*, 2006]. If resistor D is a barrier to outward flow of
768 material from beneath the Lhasa block, it must modify, but need not prohibit, channel-flow
769 extrusion of the Himalaya; channel-flow extrusion of the Greater Himalaya could be entirely
770 separate from a larger-scale flow of Tibetan crust [Klemperer, 2006]. In this case the
771 deformation patterns might more closely represent the ductile-extrusion model of Grujic *et al.*
772 [1996] than the channel-flow model of Nelson *et al.* [1996]. Beyond these caveats about the
773 way simple channel-flow models might need to be modified to operate within the constraints of
774 our MT models, we note that our MT observations only bear on the geometry of channel flow
775 (if any) today, and do not constrain the existence or nature of such flow in the Miocene that is
776 best tested against exposures of the exhumed putative channel in the Greater Himalaya
777 between the MCT and STD [Jamieson *et al.*, 2004; Kohn, 2008].

778 **9. Conclusions**

779 Re-modeling, focused inversion and hypothesis testing of two MT transects across the
780 Yarlung-Zangbo suture provide a significantly improved, and different, image of conductivity
781 from previous models (Figure 9). The new models were derived from carefully selected and
782 analyzed data, and used both the apparent resistivities and phases of both the TE and TM

783 modes, whereas the prior models by *Unsworth et al.* [2005] used only the TM-mode phases
784 and the TF data.

785 From the South Tibet Detachment to the North Himalayan gneiss domes, isolated high
786 conductivities in the upper 10 km are probably hydrothermal fluids within Tethyan Himalayan
787 sedimentary rocks, and these anomalies therefore help constrain the subsurface location of the
788 STD. Tethyan sedimentary rocks are also associated with elevated conductivity in the near-
789 surface north and south of the Kangmar Dome and above the Renbu-Zedong thrust, and
790 perhaps locally beneath the Kangmar Dome.

791 North of the Kangmar Dome and south and north of the Yalaxiangbo Dome, high
792 conductivities probably represent magma chambers and associated aqueous fluids at 10–20 km
793 depth, and their associated hydrothermal systems in the shallower crust. Other possible magma
794 chambers are present beneath the Gangdese thrust, continuing and deepening north to join the
795 well-known high-conductivity zone and presumed zone of mid-crustal partial melting beneath
796 the Gangdese batholith at ≥ 20 km depth.

797 In stark contrast to previous models published along both transects, the conductive zone
798 beneath the Gangdese batholith (Lhasa block) does not continue unbroken beneath the YZS
799 and the Tethyan Himalaya. Our new results show that the continuity of this partial-melt zone is
800 far less than indicated by our first cartoons [*Nelson et al., 1996*] and re-created as an essential
801 feature of derivative numerical models [*Beaumont et al., 2004, 2006*]. On both of our transects
802 the conductive zone is broken by a near-vertical resistor from near-surface to the base of the
803 crust that cannot have any significant melt present. This ~ 10 km wide resistive zone may
804 confine any ductile extrusion of the Himalaya to be purely south of the YZS at the present day,
805 or may prove to be discontinuous along-strike and permit a complex 3D channel-flow.

Acknowledgements

806 This work was funded by NSF Continental Dynamics grants to KDN and SLK. Many
807 scientists and students from China, U.S.A., Canada and Germany contributed to the MT
808 component of INDEPTH, in the planning stages, in the field, and during interpretation. The
809 Geological Survey of Canada is thanked for permitting AGJ to take part in INDEPTH, and for
810 making the MT equipment available. Special thanks are due to Martyn Unsworth and Larry
811 Brown. Greg Clarke and Seth Haines aided in collecting the long-period MT data on the 700
812 line. After KDN's death, JES was supervised by Paul Fitzgerald at Syracuse.

814

815 **References**

- 816 Alsdorf, D., and K.D. Nelson (1999), Tibetan satellite magnetic low: Evidence for widespread melt in the Tibetan
817 crust?, *Geology*, 27 (10), 943 - 949.
- 818 Antolín, B., E. Appel, C. Montomoli, I. Dunkl, L. Ding, R. Gloaguen, and R. El Bay (2011), Kinematic evolution
819 of the eastern Tethyan Himalaya: constraints from magnetic fabric and structural properties of the Triassic
820 flysch in SE Tibet, *Geological Society, London, Special Publications*, 349, 99–121.
- 821 Argand, E. (1924), *La Tectonique de l'Asie*, Proc. 13th Int. Geol. Cong., 1922 (Liège), 1(5), pp. 171-372.
- 822 Armijo, R., P. Tapponier, J.L. Mercier, and H. Ton-Lin (1986), Quaternary extension in southern Tibet; field
823 observations and tectonic implications, *J. Geophys. Res.*, 91, 13,803–13,872.
- 824 Bai, D. H., M.J. Unsworth, M. A. Meju, X. B. Ma, J. W. Teng, X. R. Kong, Y. Sun, J. Sun, L. F. Wang, C. S.
825 Jiang, C. P. Zhao, P. F. Xiao, and M. Liu (2010), Crustal deformation of the eastern Tibetan plateau revealed
826 by magnetotelluric imaging, *Nat. Geosci.*, 3(5), 358-362.
- 827 Bailey, R. C. (1970), Inversion of the geomagnetic induction problem, *Proceedings Royal Society London*, A315,
828 185-194.
- 829 Beaumont, C., R.A. Jamieson, M.H. Nguyen, and S. Medvedev (2004), Crustal channel flows: 1. Numerical
830 models with applications to the tectonics of the Himalayan-Tibetan orogen, *Journal of Geophysical Research*,
831 109, B06406. DOI: 10.1029/2003JB002809.
- 832 Beaumont, C., M. Nguyen, R. Jamieson and S. Ellis (2006), Crustal flow modes in large hot orogens, *Geol. Soc.*
833 *Lond. Spec. Publ.* 268, 91-145.
- 834 Bedrosian, P.A. (2007), MT+, Integrating Magnetotellurics to Determine Earth Structure, Physical State, and
835 Processes, *Surv. Geophys.*, 28, 121–167, doi 10.1007/s10712-007-9019-6
- 836 Brown, L.D., W. Zhao, K.D. Nelson, M. Hauck, D. Alsdorf, A. Ross, M. Cogan, M. Clark, X. Liu, and J. Che
837 (1996), Bright spots, structure and magmatism in Southern Tibet from INDEPTH seismic reflection profiling,
838 *Science*, 274, 1688 - 1690.
- 839 Caldwell, W., S.L. Klemperer, S.S. Rai, and J.F. Lawrence (2009), Partial melt in the upper–middle crust of the
840 northwest Himalaya revealed by Rayleigh wave dispersion, *Tectonophysics*, 477, 58–65.
- 841 Chave, A. D., and A. G. Jones (1997), Electric and magnetic field galvanic distortion decomposition of BC87
842 data, *J. Geomag. Geoelectric.*, 49(6), 767-789.
- 843 Chave, A.D., and A.G. Jones (2012), *The Magnetotelluric Method: Theory and Practice*, Cambridge University
844 Press, 575 pp., ISBN-13: 9780521819275.
- 845 Chen, Z., Y. Liu, K. V. Hodges, B. C. Burchfiel, L. Royden, and C. Deng (1990), The Kangmar Dome: A
846 metamorphic core complex in Southern Xizang (Tibet), *Science*, 250, 1552 - 1556.
- 847 Chen, L., J. Booker, A. Jones, W. Nong, M. Unsworth, W. Wei, and H. Tan (1996), Electromagnetic images of
848 colliding continents: a magnetotelluric survey of the TSangpo Suture Zone and surrounding regions, *Science*,
849 274, 1694–1696.
- 850 De Meer, S., M. R. Drury, J. H. P. De Bresser, and G. M. Pennock (2002), Current issues and new developments
851 in deformation mechanisms, rheology and tectonics, *Geol. Soc. Lond. Special Publication*, 200, 1-27.

- 852 Duba, A., S. Heikamp, W. Meurer, G. Nover, and G. Will (1994), Evidence from borehole samples for the role of
853 accessory minerals in lower-crustal conductivity, *Nature*, 367(6458), 59-61.
- 854 England, P. C., and G. A. Houseman (1986), Finite strain calculations of continental deformation; 2, Comparison
855 with the India Asia collision zone, *Journal of Geophysical Research*, 91 (3), 3664 - 3676.
- 856 Flesch, L. M., W. E. Holt, P. G. Silver, M. Stephenson, C.-Y. Wang, and W. W. Chan (2005), Constraining the
857 extent of crust-mantle coupling in central Asia using GPS, geologic, and shear-wave splitting data, *Earth and
858 Planetary Science Letters*, 238, 248–268.
- 859 Francheteau, J., C. Jaupart, J.S. Xian, K. Wen-Hua, L. De-Lu, B. Jia-Cha, W. Hung-Pin, and D. Hsia-Yeu (1984),
860 High heat flow in southern Tibet, *Nature*, 307, 32 - 36.
- 861 Groom, R.W., and Bailey, R.C., 1989. Decomposition of magnetotelluric impedance tensors in the presence of
862 local three-dimensional galvanic distortion, *Journal of Geophysical Research*, 94, 1913–192
- 863 Grujic, D., M. Casey, C. Davidson, L. S. Hollister, R. Kundig, T. Pavlis, and S. Schmid (1996), Ductile extrusion
864 of the Higher Himalayan Crystalline in Bhutan: evidence from quartz microfabrics, *Tectonophys.* 260, 21–43.
- 865 Guo, L., J. Zhang, and B. Zhang (2008), Structures, kinematics, thermochronology and tectonic evolution of the
866 Ramba gneiss dome in the northern Himalaya, *Progress in Natural Science* 18, 851–860.
- 867 Hauck, M. L., K. D. Nelson, L. D. Brown, W. Zhao, and A. Ross (1998), Crustal structure of the Himalayan
868 orogen at ~90 degrees east longitude from Project INDEPTH deep reflection profiles, *Tectonics*, 17, 481–500.
- 869 Heinson, G. S., N. G. Direen and R. M. Gill (2006), Magnetotelluric evidence for a deep-crustal mineralizing
870 system beneath the Olympic Dam iron oxide copper-gold deposit, southern Australia, *Geology*, 34, 573–576.
- 871 Henry, P., X. LePichon, and B. Goffe (1997), Kinematic, thermal and petrological model of the Himalayas:
872 constraints related to metamorphism within the underthrust Indian crust and topographic elevation,
873 *Tectonophys.*, 273, 31 - 56, 1997.
- 874 Hermance, J.F. (1979), The electrical conductivity of materials containing partial melt: a simple model from
875 Archie's law, *Geophys. Res. Lett.*, 6, 613–616.
- 876 Hetényi, G., J. Vergne, L. Bollinger, and R. Cattin (2011), Discontinuous low-velocity zones in southern Tibet
877 question the viability of the channel flow model, *Geological Society, London, Special Publications*, 353, 99–
878 108.
- 879 Hobbs, B. A. (1992), Terminology and symbols for use in studies of electromagnetic induction in the Earth, *Surv.
880 Geophys.*, 13(4-5), 489-515.
- 881 Hochstein, M. P., and Z. Yang (1992), Modeling of terrain-induced advective flow in Tibet: Implications for
882 assessment of crustal heat flow, in *Seventh Workshop on Geothermal Reservoir Engineering*, pp. 153–157,
883 Stanford Univ., Calif.
- 884 Hou, Z. Q., N. J. Cook (2009), Metallogensis of the Tibetan collisional orogen: A review and introduction to the
885 special issue. *Ore Geology Reviews* 36, 2–24.
- 886 Hou, Z. Q., Z. Q. Li (2004), Possible location for underthrusting front of the Indus continent: constraints from
887 helium isotope of the geothermal gas in southern Tibet and eastern Tibet. *Acta Geologica Sinica* 78, 482–493.
- 888 Hou, Z.Q., Z.M. Yang, X. M. Qu, X. J. Meng, Z. Q. Li, G. Beaudoin, Z. Y. Rui, Y. F. Gao (2009), The Miocene

- 889 Gangdese porphyry copper belt generated during post-collisional extension in the Tibetan Orogen. *Ore*
890 *Geology Reviews* 36, 25–51.
- 891 Jamieson R. A., C. Beaumont, S. Medvedev and M. H. Nguyen (2004), Crustal channel flows: 2. Numerical
892 models with implications for metamorphism in the Himalayan-Tibetan orogeny, *J. Geophys. Res.* 109,
893 B06407, doi:10.1029/2003JB002811.
- 894 Jamieson, R., C. Beaumont, M. Nguyen and D. Grujic (2006), Provenance of the Greater Himalayan Sequence
895 and associated rocks: predictions of channel flow models, *Geol. Soc. Lond. Spec. Publ.* 268, 165-182.
- 896 Jin, Z.-M., H. W. Green and Y. Zhou (1994), Melt topology during dynamic partial melting of peridotite, *Nature*,
897 372, 164–167.
- 898 Jones, A. G. (1983), The problem of current channelling: A critical review, *Surveys in Geophysics*, 6, 079-122.
- 899 Jones, A.G. (1992), *Electrical conductivity of the continental lower crust*. In: *Continental Lower Crust*, eds.,
900 Elsevier, Amsterdam.
- 901 Jones, A. G. (1993), The COPROD2 dataset - tectonic setting, recorded MT data, and comparison of models, *J.*
902 *Geomagn. Geoelect.*, 45(9), 933-955.
- 903 Jones, A. G., and R. W. Groom (1993), Strike angle determination from the magnetotelluric tensor in the presence
904 of noise and local distortion: rotate at you peril!, *Geophys. J. Internat.*, 113, 524-534.
- 905 Jones, A. G., and X. Garcia (2003), The Okak Bay MT dataset case study: A lesson in dimensionality and scale,
906 *Geophysics*, 68, 70–91.
- 907 Kapp, P., P. G. DeCelles, A. L. Leier, J. M. Fabijanic, S. He, A. Pullen, G. E. Gehrels, and L. Ding (2007), The
908 Gangdese retroarc thrust belt revealed, *GSA Today*, 17(7), 4-9, doi: 10.1130/GSAT01707A.1
- 909 Keranen, K.M., S.L. Klemperer, J. Julia, J.F. Lawrence and A.A. Nyblade (2009), Low lower-crustal velocity
910 across Ethiopia: is the Main Ethiopian Rift a narrow rift in a hot craton? *Geochem. Geophys. Geosyst.*, 10,
911 Q0AB01, doi:10.1029/2008GC002293, pp. 21.
- 912 Kind, R., J. Ni, W.J. Zhao, J. Wu, X. Yuan, L. Zhao, E. Sandvol, C. Reese, J. Nabelek, and T. Hearn (1996),
913 Evidence from earthquake data for a partially molten crustal layer in Southern Tibet, *Science*, 274, 1692–1694.
- 914 Klemperer, S.L., 2006. Crustal flow in Tibet: geophysical evidence for the physical state of Tibetan lithosphere,
915 and inferred patterns of active flow. In: “Channel flow, ductile extrusion and exhumation in continental
916 collision zones“, R.D., Lay, M.P. Searle and L. Godin, eds., *Geol. Soc. Lond. Special Publication*, 268, 39-70.
- 917 Kohn, M.J. (2008), P–T–t data from central Nepal support critical taper and repudiate large-scale channel flow of
918 the Greater Himalayan Sequence, *Geol. Soc. Am. Bull.*, 120, 259–273.
- 919 Ledo, J. (2005), 2-D versus 3-D magnetotelluric data interpretation, *Surveys in Geophysics*, 26(5), 511-543.
- 920 Ledo, J., A. G. Jones, I. J. Ferguson, and L. Wolyneec (2004), Lithospheric structure of the Yukon, northern
921 Canadian Cordillera, obtained from magnetotelluric data, *J. Geophys. Res.*, 109(B4), B04410, doi:
922 10.1029/2003JB002516.
- 923 Lee, J., B. R. Hacker, W. S. Dinklage, Y. Wang, P. Gans, A. Calvert, J. Wan, W. Chen, A. E. Blythe, and W.
924 McClelland (2000), Evolution of the Kangmar Dome, southern Tibet: Structural, petrologic, and
925 thermochronologic constraints, *Tectonics*, 19(5), 872–895.

- 926 Leech, M.L. (2008), Does the Karakoram fault interrupt mid-crustal channel flow in the western Himalaya? *Earth*
927 *Planet. Sci. Lett.*, 276, 314-322, doi:10.1016/j.epsl.2008.10.006.
- 928 Leech, M.L., S. Singh, A.K. Jain, S.L. Klemperer, and R.M. Manickavasagam (2005), The onset of India-Asia
929 continental collision: early, steep subduction required by the timing of UHP metamorphism in the western
930 Himalaya, *Earth Planet. Sci. Lett.*, 234, 83-97.
- 931 Le Pape, F., A.G. Jones, J. Vozar, and W. Wei (2012), Penetration of crustal melt beyond the Kunlun Fault into
932 northern Tibet, *Nature Geoscience*, 5, 330-335, doi: 10.1038/NCEO1449.
- 933 Li, S., M.J. Unsworth, J.R. Booker, W. Wei, H. Tan, and A.G. Jones (2003), Partial melt or aqueous fluid in the
934 mid-crust of southern Tibet? Constraints from INDEPTH magnetotelluric data, *Geophys. J. Internat.*, 153,
935 289-305.
- 936 Li, G., K. Qin, K. Ding, T. Liu, J. Li, S. Wang, S. Jiang and S. Zhang (2006), Geology, Ar-Ar Age and Mineral
937 Assemblage of Eocene Skarn Cu-Au±Mo Deposits in the Southeastern Gangdese Arc, Southern Tibet:
938 Implications for Deep Exploration. *Resource Geology* 56, 315–336.
- 939 Long, S.P., McQuarrie, N., Tobgay, T., Grujic, D. and Hollister, L. (2011) Geologic Map of Bhutan, *Journal of*
940 *Maps*, 2011, 184–192. doi:10.4113/jom.2011.1159.
- 941 Livelybrooks, D., M. Mareschal, E. Blais, and J. T. Smith (1996), Magnetotelluric delineation of the Trillabelle
942 massive sulfide body in Sudbury, Ontario, *Geophysics*, 61, 970–986.
- 943 Mackie, R.L., and T.R. Madden (1993), Three-dimensional magnetotelluric inversion using conjugate gradients,
944 *Geophys. J. Internat.*, 115, 215 - 229.
- 945 Makovsky, Y., S. L. Klemperer, L. Huang, D. Lu, and Project INDEPTH Team (1996a), Structural elements of
946 the southern Tethyan Himalaya crust from wide-angle seismic data, *Tectonics*, 15, 997-1005.
- 947 Makovsky, Y., S. L. Klemperer, L. Ratschbacher, L.D. Brown, M. Li, W. Zhao and F. Meng (1996b), INDEPTH
948 wide-angle reflection observation of P-wave-to-S-wave conversion from crustal bright spots in Tibet, *Science*,
949 274, 1690-1691.
- 950 Makovsky, Y., and S. Klemperer (1999), Measuring the seismic properties of Tibetan bright spots: Evidence for
951 free aqueous fluids in the Tibetan middle crust, *J. Geophys. Res.*, 104, 10,795–10,825,
- 952 Makovsky, Y., S. L. Klemperer, L. Ratschbacher, and D. Alsdorf (1999), Midcrustal reflector on INDEPTH wide-
953 angle profiles: An ophiolite slab beneath the India-Asia suture in southern Tibet?, *Tectonics*, 18, 793–808.
- 954 Mechie, J., R. Kind, and J. Saul (2011), The seismological structure of the Tibetan Plateau crust and mantle down
955 to 700 km depth, *Geological Society, London, Special Publications*, 353, 109–125.
- 956 Meyerhoff, A. A., I. Taner, and M. Kamen-Kaye (1986), The Indus-Yarlung Fault Zone: a Confusion of Terms,
957 *Episodes*, 9(2), 103.
- 958 Nelson, K.D., W. Zhao, L.D. Brown, J. Kuo, J. Che, X. Liu, S.L. Klemperer, Y. Makovsky, R. Meissner, J.
959 Mechie, R. Kind, F. Wenzel, J. Ni, J. Nabelek, L. Chen, H. Tan, W. Wei, A. G. Jones, J. Booker, M.
960 Unsworth, W. S. F. Kidd, M. Hauck, D. Alsdorf, A. Ross, M. Cogan, C. Wu, E. Sandvol, M. Edwards (1996),
961 Partially molten middle crust beneath southern Tibet; synthesis of Project INDEPTH results, *Science*, 274,
962 1684 - 1688.

- 963 Pan, G., J. Ding, D. Yao, and L. Wang (2004), Geological Map of Qinghai-Xizang (Tibet) Plateau and Adjacent
964 Areas (1:1,500,000). Chengdu Institute of Geology and Mineral Resources, China Geological Survey.
965 Chengdu Cartographic Publishing House.
- 966 Parker, R.L., and J. R. Booker (1996), Optimal one-dimensional inversion and bounding of magnetotelluric
967 apparent resistivity and phase measurements, *Phys. Earth, Planet. Inter.*, 98, 269 - 282.
- 968 Partzsch, G.M., F.R. Schilling, and J. Arndt (2000), The influence of partial melting on the electrical behavior of
969 crustal rocks: laboratory examination, model calculations and geological interpretations, *Tectonophys.*, 317,
970 189–203.
- 971 Pham, V. N., D. Boyer, P. Therme, X. C. Yuan, L. Li, and G. Y. Jin (1986), Partial melting zones in the crust of
972 southern Tibet from magnetotelluric results, *Nature*, 319, 310 - 314.
- 973 Pommier, A., F. Gaillard, M. Malki, and M. Pichavant (2010), Methodological re-evaluation of the electrical
974 conductivity of silicate melts, *Am. Miner.*, 95(2-3), 284-291.
- 975 Pommier, A., and E. Le-Trong (2011), "SIGMELTS": A web portal for electrical conductivity calculations in
976 geosciences, *Comput. Geosci.*, 37(9), 1450-1459.
- 977 Qi, X. X., T. F. Li, X. J. Meng, C. L. Yu (2008), Cenozoic tectonic evolution of the Tethyan Himalayan foreland
978 fault-fold belt in southern Tibet, and its constraint on antimony-gold polymetallic minerogenesis. *Acta*
979 *Petrologica Sinica* 24, 1638-1648.
- 980 Rippe, D., and M. Unsworth (2010), Quantifying crustal flow in Tibet with magnetotelluric data, *Physics of the*
981 *Earth and Planetary Interiors*, 179(3-4), 107-121.
- 982 Rodi, W., and R. L. Mackie (2001), Nonlinear conjugate gradients algorithm for 2-D magnetotelluric inversion,
983 *Geophysics*, 66, 174-186.
- 984 Rosenberg, C. L., and M. R. Handy, (2005), Experimental deformation of partially melted granite revisited:
985 Implications for the continental crust, *Journal of Metamorphic Geology*, 23, 19–28. doi:10.1111/j.1525-
986 1314.2005.00555.x.
- 987 Schilling, F. R., G. M. Partzsch, H. Brasse, and G. Schwarz (1997), Partial melting below the magmatic arc in the
988 central Andes deduced from geoelectromagnetic field experiments and laboratory data, *Phys. Earth Planet.*
989 *Inter.*, 103, 17-31.
- 990 Shen, F., L. Royden, and B.C. Burchfiel (2001), Large-scale crustal deformation of the Tibetan Plateau, *J.*
991 *Geophys. Res.*, 106, 6793 - 6816.
- 992 Solon, K. D., et al. (2005), Structure of the crust in the vicinity of the Banggong-Nujiang suture in central Tibet
993 from INDEPTH magnetotelluric data, *J. Geophys. Res.*, 110(B10102), B10102, doi: 10.1029/2003JB002405.
- 994 Spratt, J. E., A. G. Jones, K. D. Nelson, M. J. Unsworth, and the INDEPTH team (2005). Crustal structure of the
995 India-Asia collision zone, southern Tibet, from INDEPTH MT investigations, *Physics of the Earth and*
996 *Planetary Interiors*, 150, 227-237.
- 997 Schwalenberg, K., V. Rath, and V. Haak (2002), Sensitivity studies applied to a two-dimensional resistivity model
998 from the Central Andes, *Geophys. J. Internat.*, 150(3), 673-686.
- 999 Tozer, D. C. (1979), The interpretation of upper-mantle electrical conductivities, *Tectonophysics*, 56, 147-163.

- 1000 Unsworth, M. J., A. G. Jones, W. Wei, G. Marquis, S. G. Gokarn, J. E. Spratt, and the INDEPTH-MT team
1001 (2005), Crustal rheology of the Himalaya and Southern Tibet inferred from magnetotelluric data, *Nature*, *438*,
1002 78-81, doi: 10.1038/nature04154.
- 1003 Wannamaker, P. E., T. G. Caldwell, G. R. Jiracek, V. Maris, G. J. Hill, Y. Ogawa, H. M. Bibby, S. L. Bennie, and
1004 W. Heise (2009), Fluid and deformation regime of an advancing subduction system at Marlborough, New
1005 Zealand, *Nature*, *460*, 733–736.
- 1006 Wannamaker, P. E., G. W. Hohmann, and S. H. Ward (1984), Magnetotelluric responses of 3-dimensional bodies
1007 in layered Earths, *Geophysics*, *49*(9), 1517-1533.
- 1008 Weckmann, U., O. Ritter, A. Jung, T. Branch, and M. de Wit (2007), Magnetotelluric measurements across the
1009 Beattie magnetic anomaly and the Southern Cape Conductive Belt, South Africa, *J. Geophys. Res.*, *112*,
1010 B05416, doi:10.1029/2005JB003975.
- 1011 Wei, W., M. Unsworth, A. G. Jones, H. Tan, K.D. Nelson, J. Booker, L. Chen, L. Li, K. Solon, P. Bedrosian, S.
1012 Jin, and M. Deng (2001), Detection of widespread fluids in the Tibetan crust, *Science*, *292*, 716 - 718.
- 1013 Wei, W., S. Jin, G. Ye, M. Deng, J. Jing, M. Unsworth, A.G. Jones, (2010), Conductivity structure and
1014 rheological property of lithosphere in Southern Tibet inferred from super-broadband magnetotelluric sounding,
1015 *Science in China Series D: Earth Sciences*, *53*, 1–14.
- 1016 Yang, Z. S., Z. Q. Hou, X. J. Meng, Y. C. Liu, H. C. Fei, S. H. Tian, Z. Q. Li, and W. Gao (2009), Post-collisional
1017 Sb and Au mineralization related to the South Tibetan detachment system, Himalayan orogen. *Ore Geology*
1018 *Reviews* *36*, 194–212.
- 1019 Yin, A. (2006), Cenozoic tectonic evolution of the Himalayan orogen as constrained by along-strike variation of
1020 structural geometry, exhumation history, and foreland sedimentation, *Earth Science Reviews*, *76*, 1-131,
1021 doi:10.1016/j.earscirev.2005.05.004.
- 1022 Yin, A., T. M. Harrison, F. J. Ryerson, C. Wenji, W. S. F. Kidd, and P. Copeland (1994), Tertiary structural
1023 evolution of the Gangdese thrust system, southeastern Tibet, *J. Geophys. Res.*, *99*, 18,175 - 18,201.
- 1024 Yin, A., T. M. Harrison, M. A. Murphy, M. Grove, S. Nie, F. J. Ryerson, W. X. Feng, and C. Z. Le (1999),
1025 Tertiary deformation history of southeastern and southwestern Tibet during the Indo-Asian collision, *Geol.*
1026 *Soc. Am. Bull.* *111*, 1644–1664.
- 1027 Yin, A., C. S. Dubey, T. K. Kelty, A. A. G. Webb, T. M. Harrison, C. Y. Chou, and J. C  lerier, (2010), Geologic
1028 correlation of the Himalayan orogen and Indian craton (part 2): Structural geology, geochronology, and
1029 tectonic evolution of the Eastern Himalaya, *Geol. Soc. Am. Bull.*, *122*, 360-395.
- 1030 Zeng, L., L. Gao, K. Xie, and J. Liu-Zeng (2011) Mid-Eocene high Sr/Y granites in the Northern Himalayan
1031 Gneiss Domes: Melting thickened lower continental crust, *Earth Planet. Sci. Lett.*, *303*, 251–266
- 1032 Zhao, W., and W. J. Morgan (1987), Injection of Indian crust into Tibetan lower crust: A two-dimensional finite
1033 element model study, *Tectonics*, *6*, 489 - 504.
- 1034 Zhao, W., K. D. Nelson, J. Che, J. Guo, D. Lu, C. Wu, X. Liu, L.D. Brown, M. Hauck, J. T. Kuo, S. L.
1035 Klemperer, and Y. Makovsky (1993), Deep seismic reflection evidence for continental underthrusting beneath
1036 southern Tibet, *Nature*, *366*, 557 - 559.

- 1037 Zhao, W. J., J. Mechie, J. Guo, F. Wenzel, R. Meissner, L. Ratschbacher, H. Steentoft, S. Husen, H.-J. Brauner,
1038 D. Jiang, W. Frisch, and S.-F. Hauff (1997). Seismic mapping of crustal structures beneath the Indus-Yarlung
1039 suture, Tibet, *Terra Nova* 9, 42–46.
- 1040 Zhao, W., J. Mechie, L.D. Brown, J. Guo, S. Haines, T. Hearn, S. L. Klemperer, Y. S. Ma, R. Meissner, K. D.
1041 Nelson, J. Ni, P. Pananont, R. Rapine, A. Ross, and J. Saul (2001), Crustal structure of central Tibet as derived
1042 from project INDEPTH wide-angle seismic data, *Geophys. J. Internat.*, 156, 486–498.

1043 Figure captions

1044 **Figure 1.** (a) Terrane map of the Tibetan Plateau and INDEPTH magnetotelluric profiles, showing location of
 1045 Figure 2. (b) Cross-section of the Himalaya and southern Tibetan Plateau, modified from *Nelson et al.* [1996]
 1046 (vertical exaggeration ~130%). MFT–Main Frontal Thrust; MBT–Main Boundary Thrust; MCT–Main Central
 1047 Thrust; MHT– Main Himalayan Thrust; STD–South Tibetan Detachment; YZS–Yarlung-Zangbo Suture; Ybj–
 1048 Yangbajian graben; BNS–Banggong-Nujiang Suture.

1049
 1050 **Figure 2.** MT site locations along 100- and 700-lines across the Yarlung-Zangbo suture in Southern Tibet. Yellow
 1051 squares show the location of data used in focused inversions (Figures 7 and 8). LT–Lhunze thrust; RZT–
 1052 Renbu-Zedong thrust; GT–Gangdese thrust; KD–Kangmar dome; RB–Renbu dome; YXD–Yalaxiangbo
 1053 dome; all other abbreviations as in Figure 1. Geology from *Pan et al.* [2004]; *Yin* [2006]; *Antolin et al.* [2011];
 1054 *Long et al.* [2011]; *Zeng et al.* [2011]. Heat-flow measurements from *Francheteau et al.* [1984]; Sino-French
 1055 MT recording sites from *Pham et al.* [1986]; reflection profiles and seismic reflection bright spots from *Brown*
 1056 *et al.* [1996] and *Hauck et al.* [1998]; geothermal manifestations from *Hou and Li* [2004]; mineral deposits
 1057 from *Li et al.* [2006], *Qi et al.* [2008], *Hou et al.* [2009] and *Yang et al.* [2009].

1058
 1059 **Figure 3.** Conductivity models for the 100-line profile, re-plotted with a uniform resistivity color scale, from (a)
 1060 *Chen et al.* [1996], (b) *Wei et al.* [2001], (c) *Unsworth et al.* [2005], (d) preferred model (this paper). Reds
 1061 represent regions of high conductivity and blues represent resistive regions. Five major first-order features also
 1062 recognized on the 700-profile (Figure 4) are three conductive zones (A, B, and C) and two resistive regions (D
 1063 and B). Dashed boxes show the areas selected for focused inversions in Figure 7. Black triangles mark
 1064 recording locations. (Sites 121, 165 and 175 (Figure 2) were not used in the inversion in (d) as in this line of
 1065 projection they are closer to the adjacent station than the inversion mesh size.) Pseudosections show the phase
 1066 difference between the observed data and the model response in (e) the TE-mode and (f) the TM-mode.

1067
 1068 **Figure 4.** Conductivity models for the 700-line profile. (a) *Unsworth et al.* [2005], (b) preferred model, this paper
 1069 (modified from *Spratt et al.* [2005]). (Site 780 (Figure 2) was not used in the inversion in (b) as in this line of
 1070 projection it is closer to the adjacent station than the inversion mesh size.) Dashed boxes show the areas
 1071 selected for focused inversions in Figure 8. Pseudosections show the phase difference between the observed
 1072 data and the model response in (c) the TE-mode and (d) the TM-mode.

1073
 1074 **Figure 5.** Hypothesis testing of the 700-line model. Specific resistivity values are altered, and pseudosections are
 1075 plotted of the phase difference between our preferred model (Figure 4b) and the altered model, in both the TE-
 1076 mode and the TM-mode. (a) Adding a resistive block (dark purple) beneath the high conductivity zone (C)
 1077 results in no significant differences between the phases in either the TE- or TM-modes, indicating our data are
 1078 insensitive to the deep structure north of the YZS. (b) Connecting the two mid-crustal conductors B and C
 1079 with conductive material (yellow-orange) across resistor D results in large differences in the phases in the TM

1080 mode. (c) Altering the resistivity values below conductors A and B to match those observed within feature D
 1081 yields no significant phase differences, showing that the deeper crust here could be more resistive than shown
 1082 in the final model.

1083

1084 **Figure 6.** Hypothesis testing of the 100-line model. (a) Replacing the shallow part of conductor C with a resistor
 1085 linking D and E. (b) Connecting conductors B and C with a conductor that cuts across resistor D (analogous to
 1086 Figure 5b). (c) Continuing conductor C to the surface south of the YSZ and again cutting across resistor D.
 1087 The RMS value increases significantly in each case and significant phase differences are observed, particularly
 1088 in the TM-mode.

1089

1090 **Figure 7** Focused models of upper-crustal conductivity structure along the 100-line profile. Letters A, B, C, D
 1091 mark the same distinctive features as in Figure 3. Black lines mark the location of fault zones and seismic
 1092 reflectors taken directly from other papers, dashed where confidently imaged or from constrained geologic
 1093 cross-sections, dotted where extrapolated or from schematic or cartoon cross-sections. (a) Focused model
 1094 across the southern end of the 100-line. Mesh has 41 rows and 145 columns. Dashed line is STD interpreted
 1095 from INDEPTH reflection data [*Hauck et al.*, 1998]. (b) Focused model across the Kangmar dome. Mesh has
 1096 41 rows and 145 columns. Dashed line above 10 km depth is boundary between Kangmar gneisses (Greater
 1097 Himalayan Sequence, GH) and sedimentary rocks (Tethyan Himalaya, TH) from structural cross-section of
 1098 *Lee et al.* [2000] that is “interpretative and schematic” below about 3 km depth. Dashed lines below 10 km
 1099 depth are prominent reflections beneath the Kangmar dome (imaged ~20 km east), and a bright spot of the
 1100 “Yamdrok-Damxung reflection band” (imaged ~50 km east) from INDEPTH reflection data [*Brown et al.*,
 1101 1996; *Hauck et al.*, 1998]. (c) focused model across the YZS. Mesh consists of 51 rows and 126 columns.
 1102 Dotted lines are Renbu-Zedong thrust (RZT) and Gangdese thrust (GT) from the cartoon by *Makovsky et al.*
 1103 [1999], and (shallower dotted line at south end) schematic STD from *Lee et al.* [2000]; dashed lines at depth
 1104 bound the “Yarlung Zangbo reflector” from INDEPTH wide-angle seismic data [*Makovsky et al.*, 1999],
 1105 dotted where not clearly imaged.

1106

1107 **Figure 8** Focused models of upper-crustal conductivity structure along the 700-line profile. (a) Focused model
 1108 across the STD. Mesh is 50 rows and 106 columns. Dotted line is speculative STD, following geometry along
 1109 100-line [*Hauck et al.*, 1998] (Figure 7a) extrapolated 200 km to the east. (b) Focused model across the
 1110 Lhunze thrust and Yalaxiangbo dome. Mesh is 51 rows and 141 columns. Dotted line is speculative STD
 1111 (upper boundary of Yalaxiangbo dome) following geometry along 100-line, extrapolated 200 km to the east.
 1112 (c) Focused model across YZS. Mesh is 41 rows and 142 columns. Dashed lines are RZT and GT from
 1113 structural cross-section of *Yin et al.* [1994, 1999]; dotted line is speculative upper boundary of Yalaxiangbo
 1114 dome from *Lee et al.* [2000] (Figure 7b) and *Yin et al.* [2010].

1115

1116 **Figure 9** Conductivity model and geologic interpretation of (a) 100- and (b) 700-line MT profiles in southern
1117 Tibet, with no vertical exaggeration. Conductive zone A is interpreted as geothermal fluids; conductors C as
1118 regions of partial melt; and conductive zones B as magma in some areas and water in others.

Figure 1

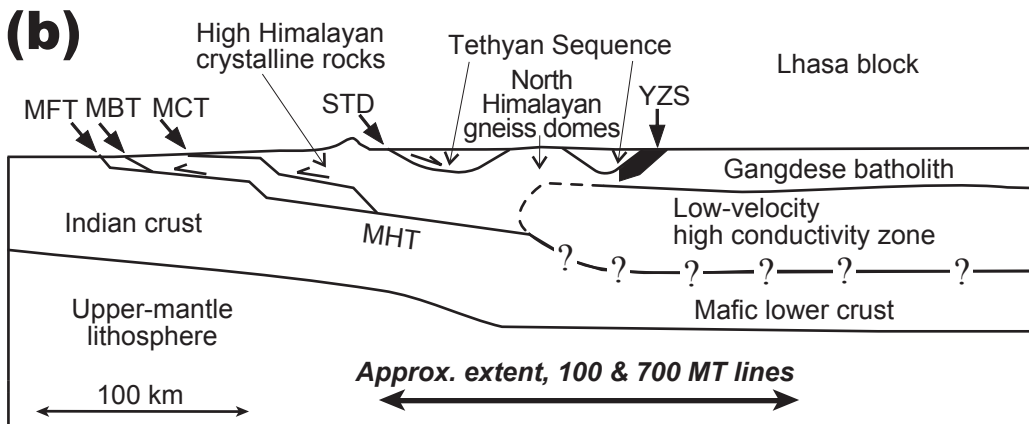
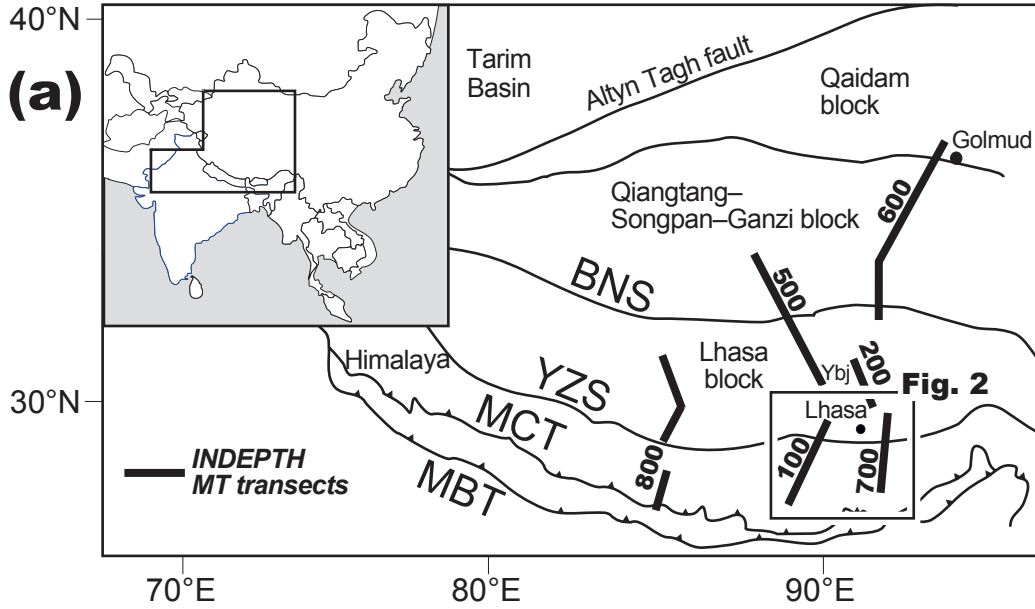
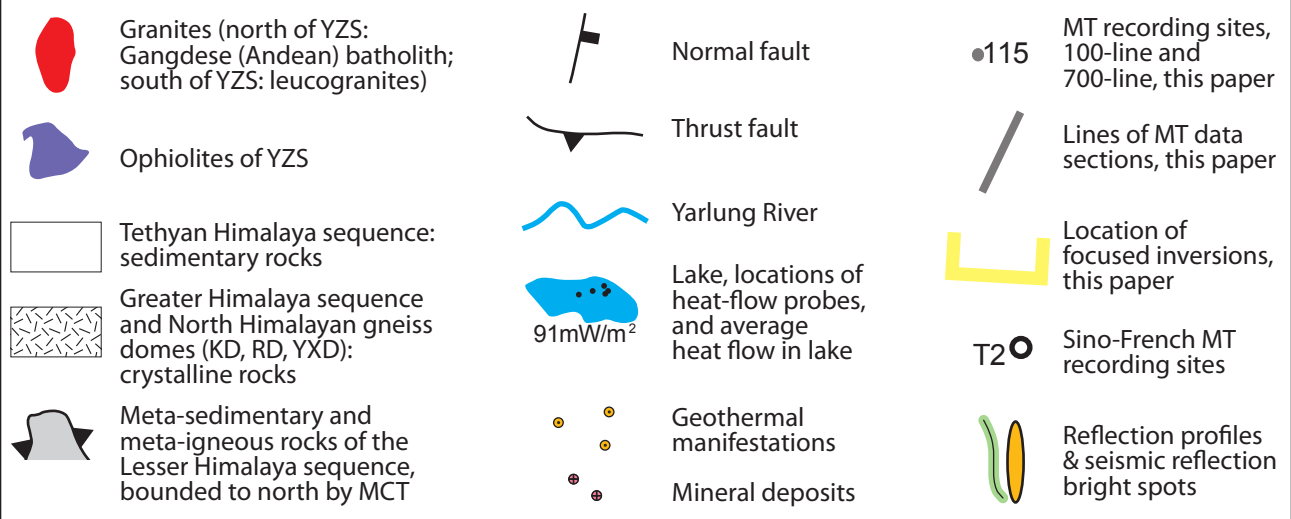
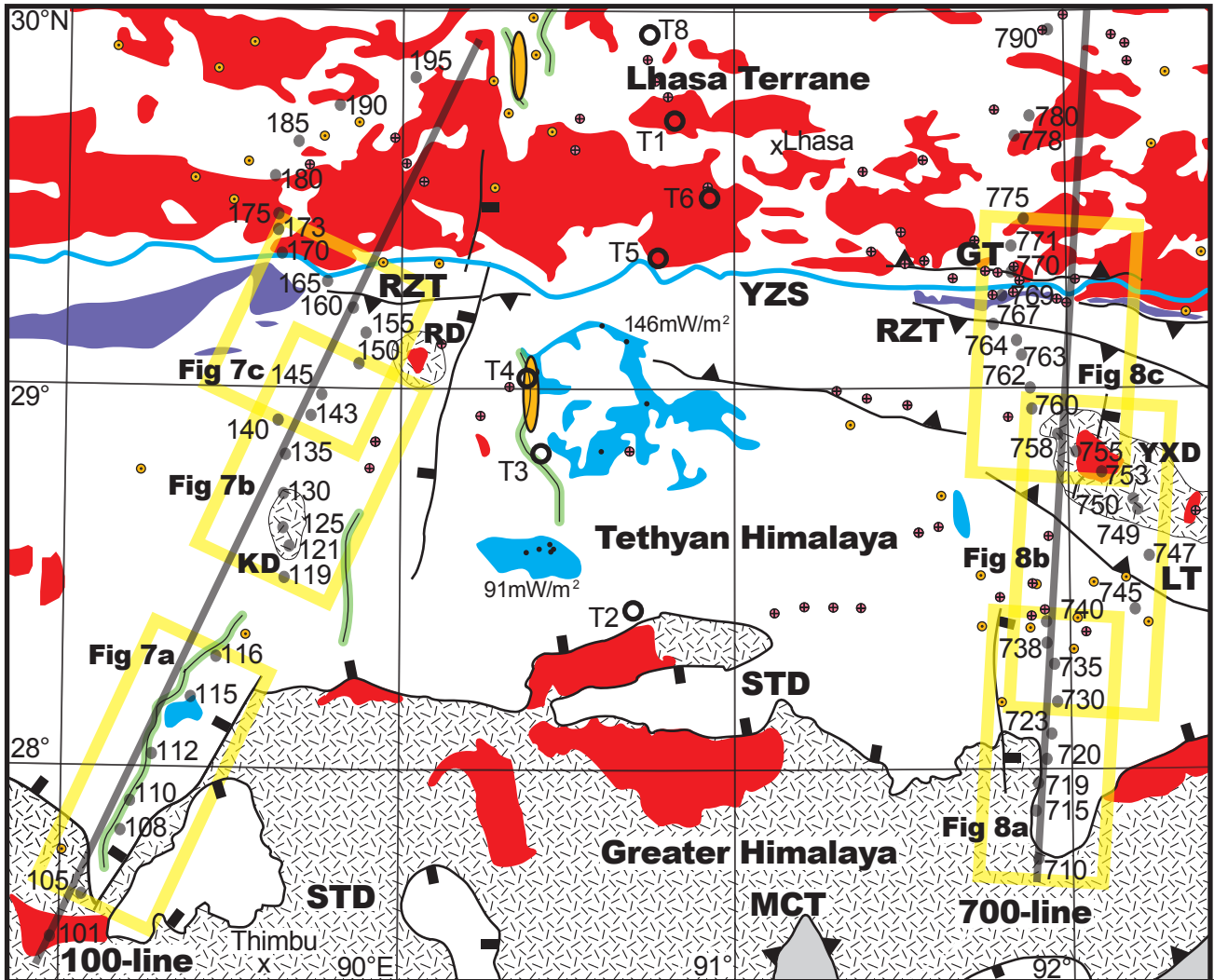


Figure 2



100-line

Figure 3

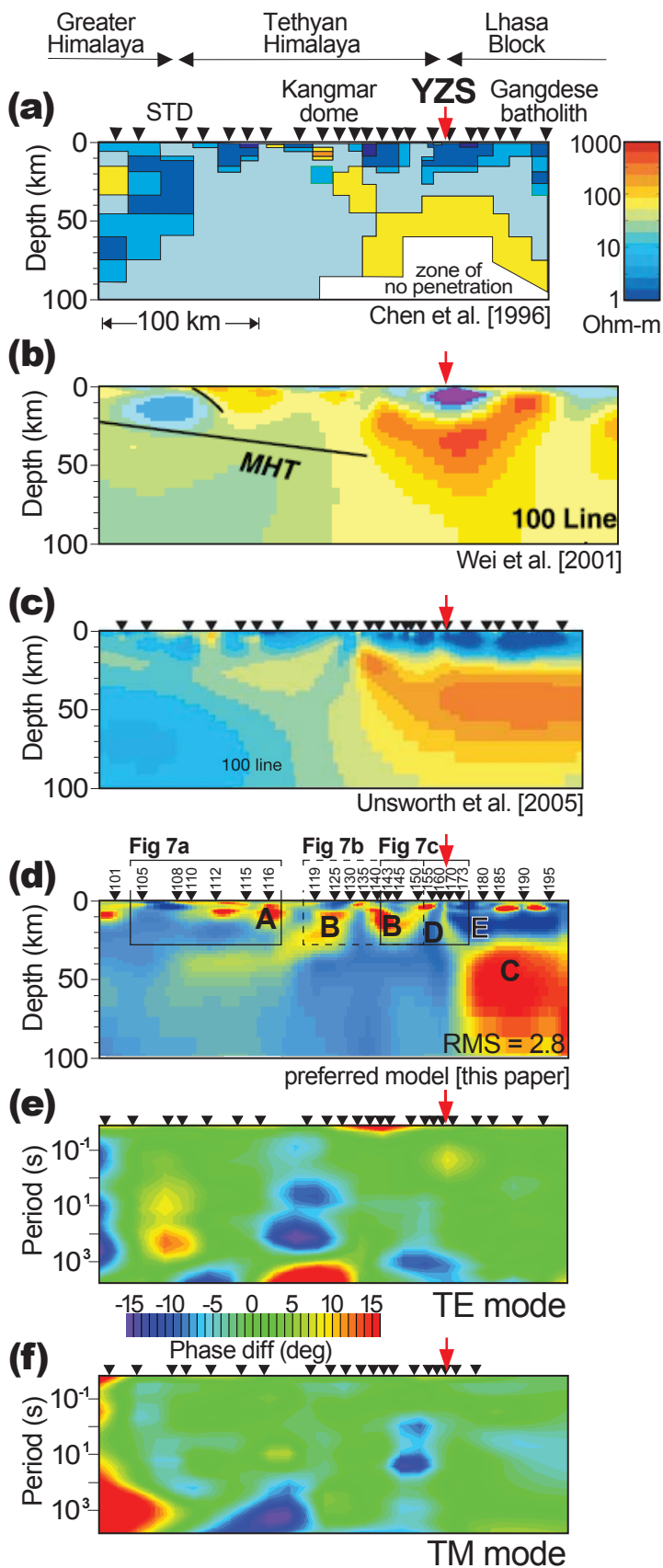


Figure 4

700-line

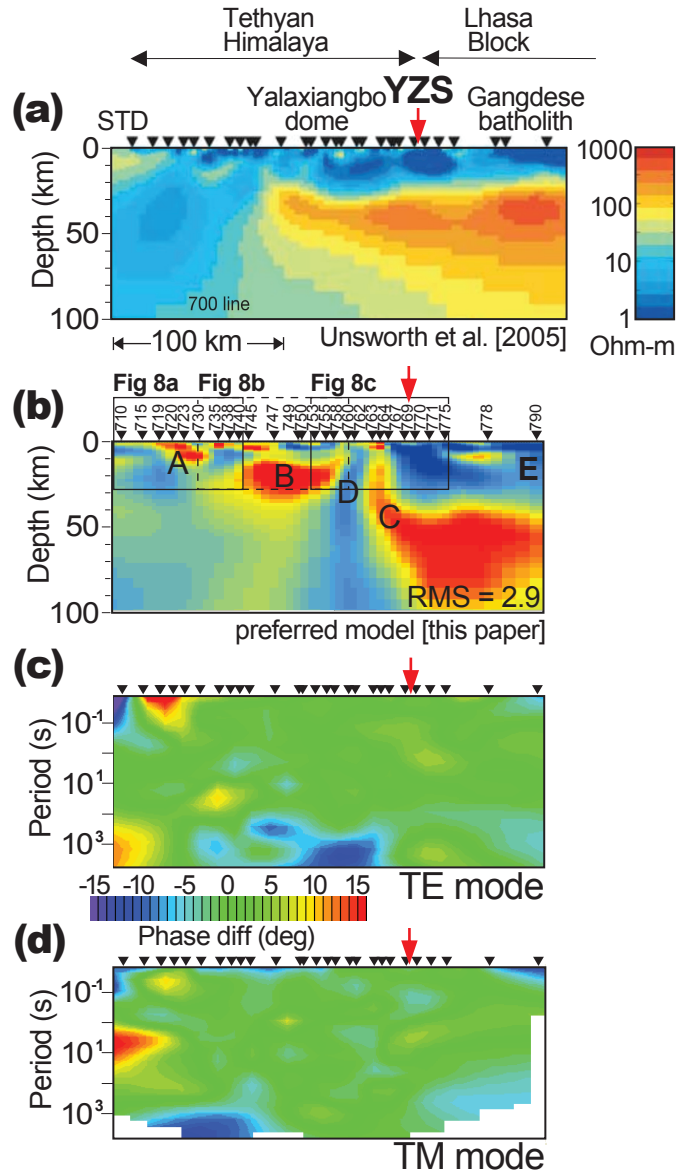


Figure 5

700-line

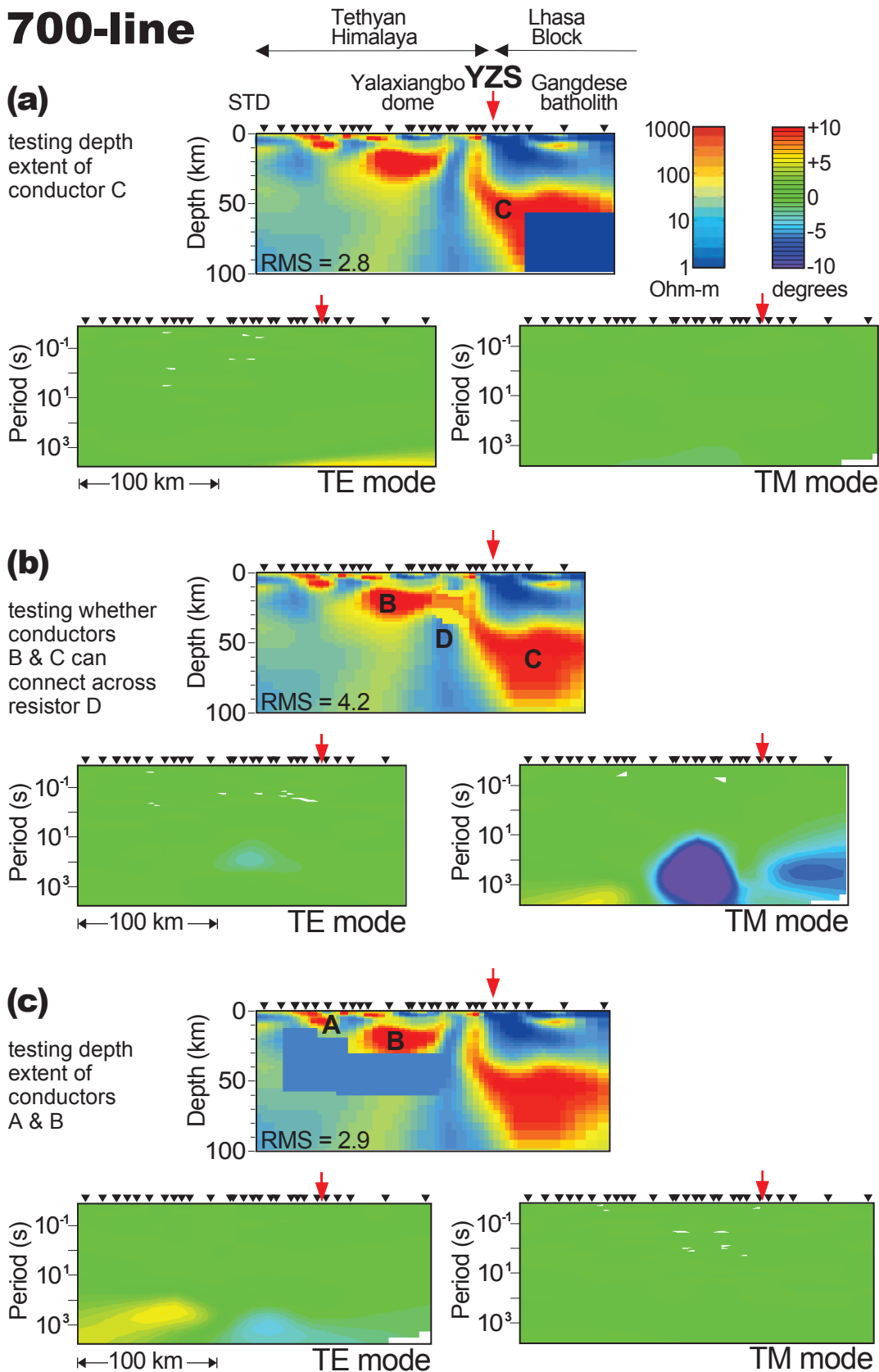
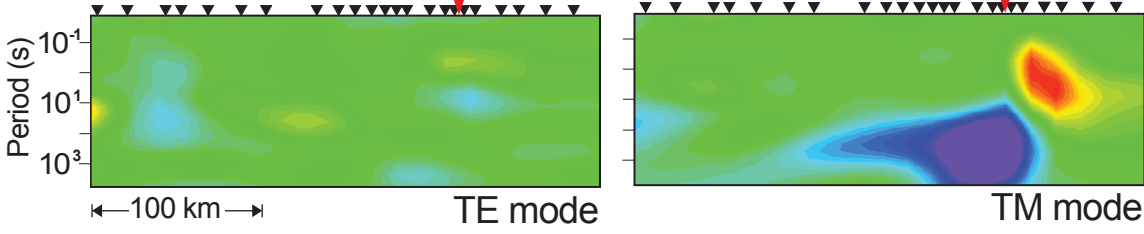
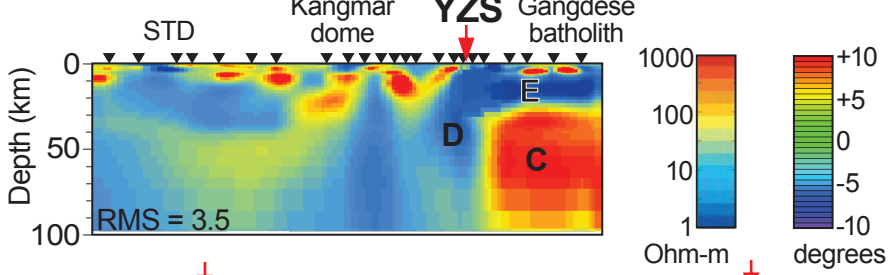


Figure 6

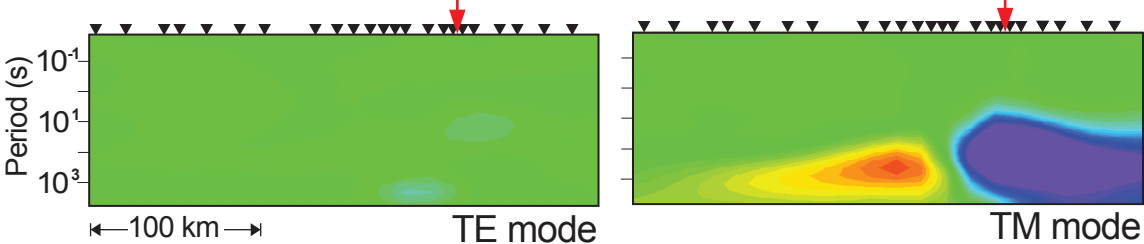
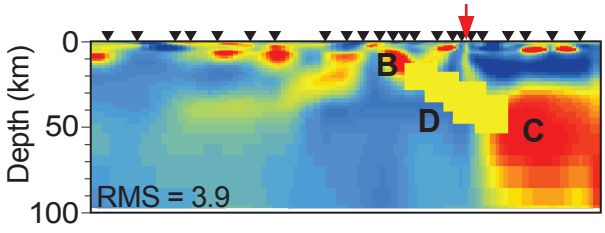
100-line



(a)
testing whether resistors D & E can connect across conductor C



(b)
testing whether conductors B & C can connect across resistor D



(c)
testing whether conductor C can extend to the surface, cutting across resistor D

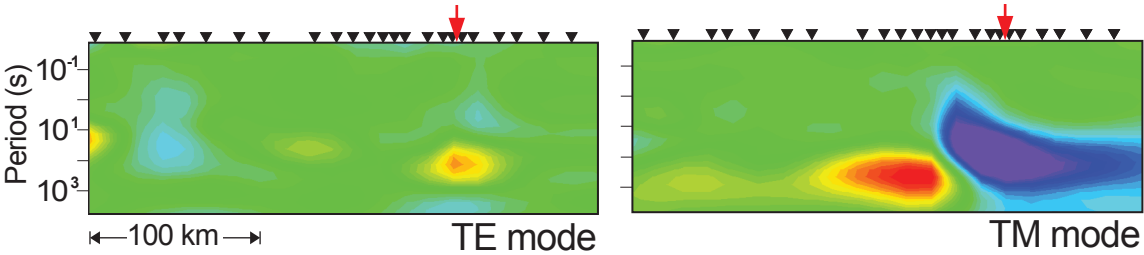
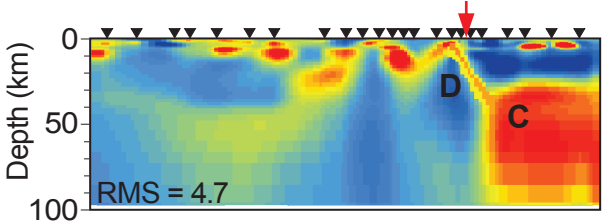


Figure 7

100-line

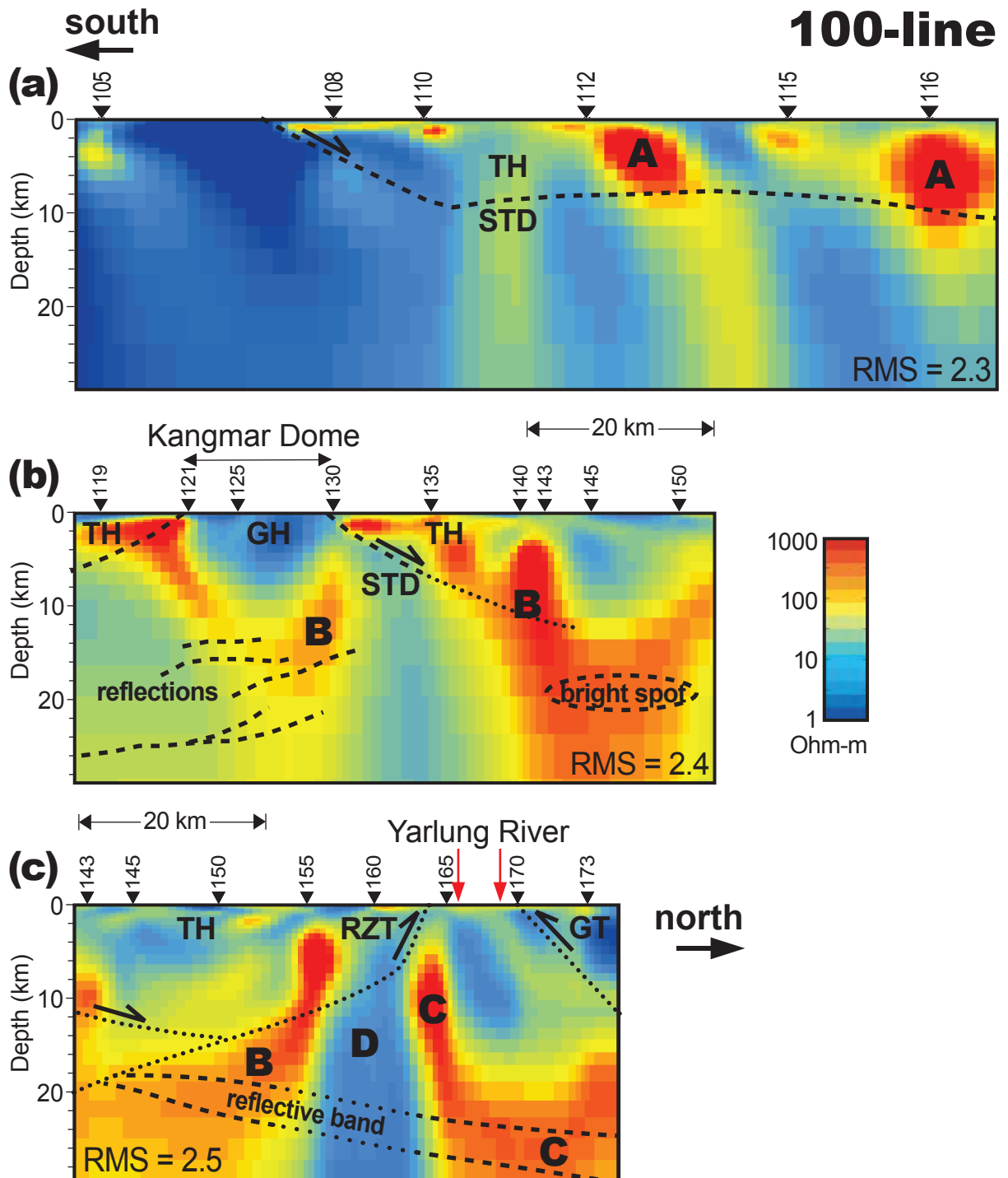


Figure 8

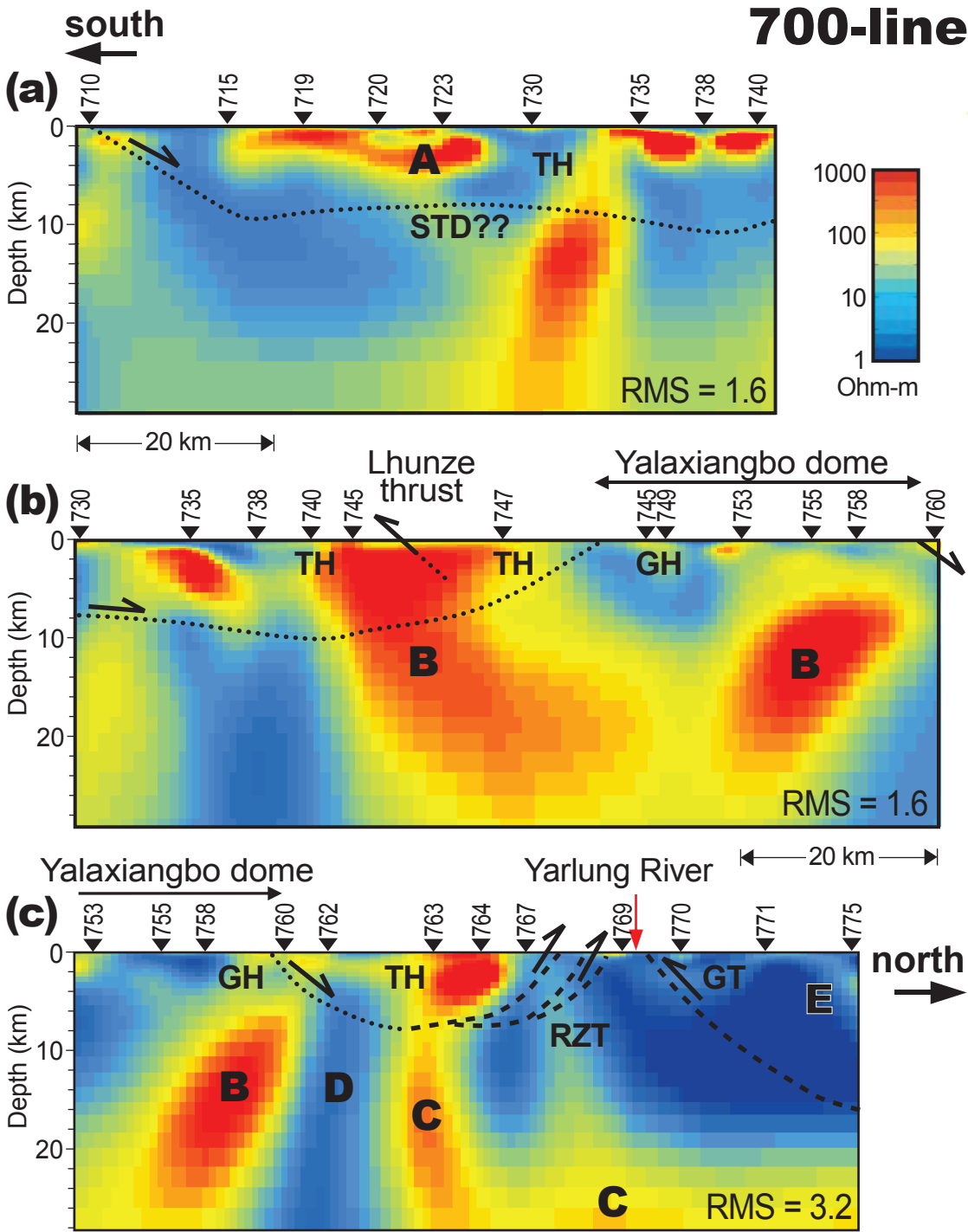


Figure 9

